Key Points:
- CAM6 and E3SM show similar liquid water content (LWC) and ice water content (IWC) compared to observations from −25°C to 0°C, but show higher (lower) LWC (IWC) at lower temperatures
- Higher LWC, IWC, N_{liq}, and N_{ice} were observed with higher aerosol concentrations, yet such correlations are weaker in models
- CAM6 shows the most similar ice, liquid, and mixed phase frequency compared to 100-km observations; CAM5 and E3SM show less similarity

Correspondence to:
M. Diao,
minghui.diao@sjsu.edu

Author Contributions:
Conceptualization: Minghui Diao
Data curation: Ching An Yang, Minghui Diao, Andrew Gettelman, Kai Zhang, Jian Sun, Greg McFarquhar, Wei Wu
Formal analysis: Ching An Yang, Minghui Diao
Funding acquisition: Minghui Diao
Investigation: Ching An Yang, Minghui Diao
Methodology: Ching An Yang, Minghui Diao

Ice and Supercooled Liquid Water Distributions Over the Southern Ocean Based on In Situ Observations and Climate Model Simulations

Ching An Yang[1] [ID], **Minghui Diao[1]** [ID], **Andrew Gettelman[2]** [ID], **Kai Zhang[3]** [ID], **Jian Sun[3,4]** [ID], **Greg McFarquhar[5,6]** [ID], **and Wei Wu[5]** [ID]

[1]Department of Meteorology and Climate Science, San Jose State University, San Jose, CA, USA, [2]National Center for Atmospheric Research, Boulder, CO, USA, [3]Pacific Northwest National Laboratory, Richland, WA, USA, [4]Computational & Information Systems Laboratory, National Center for Atmospheric Research, Boulder, CO, USA, [5]Cooperative Institute for Severe and High Impact Weather Research and Operations, University of Oklahoma, Norman, OK, USA, [6]School of Meteorology, University of Oklahoma, Norman, OK, USA

Abstract Three climate models are evaluated using in situ airborne observations from the Southern Ocean Clouds, Radiation, Aerosol Transport Experimental Study (SOCRATES) campaign. The evaluation targets cloud phases, microphysical properties, thermodynamic conditions, and aerosol indirect effects from −40°C to 0°C. Compared with 580-s averaged observations (i.e., 100 km horizontal scale), the Community Atmosphere Model version 6 (CAM6) shows the most similar result for cloud phase frequency distribution and allows more liquid-containing clouds below −10°C compared with its predecessor—CAM5. The Energy Exascale Earth System Model (E3SM) underestimates (overestimates) ice phase frequencies below (above) −20°C. CAM6 and E3SM show liquid and ice water contents (i.e., LWC and IWC) similar to observations from −25°C to 0°C, but higher LWC and lower IWC than observations at lower temperatures. Simulated in-cloud RH shows higher minimum values than observations, possibly restricting ice growth during sedimentation. As number concentrations of aerosols larger than 500 nm (Na_{500}) increase, observations show increases of LWC, IWC, liquid, and ice number concentrations (N_{liq}, N_{ice}). Number concentrations of aerosols larger than 100 nm (Na_{100}) only show positive correlations with LWC and N_{liq}. From −20°C to 0°C, higher aerosol number concentrations are correlated with lower glaciation ratio and higher cloud fraction. From −40°C to −20°C, large aerosols show positive correlations with glaciation ratio. CAM6 shows small increases of LWC and N_{liq} with Na_{500} and Na_{100}. E3SM shows small increases of N_{ice} with Na_{500}. Overall, CAM6 and E3SM underestimate aerosol indirect effects on ice crystals and supercooled liquid droplets over the Southern Ocean.

Plain Language Summary Clouds can be collections of entirely liquid droplets, ice particles, or both. Whether clouds are liquid, ice, or a mixture, particularly over the Southern Ocean, contributes to large uncertainties in climate model simulations. This study uses aircraft observations to evaluate the performance of three climate models. The evaluation compares model simulations with the observation data in terms of environmental conditions (temperature and relative humidity), small-scale properties (amount of liquid and ice), and the relationship between aerosols and clouds at temperatures from −40°C to 0°C. A commonly used model (CAM5) does not allow supercooled liquid water at temperatures <−10°C, while a newer version of it (CAM6), produces distributions of the three cloud phases comparable to observations. Another climate model (E3SM), on the other hand, produces too many liquid clouds and too few ice clouds from −35°C to −20°C. CAM6 and E3SM show an insufficient amount of ice and a surplus of supercooled liquid water compared with observations between −40°C and −25°C. As aerosol number concentrations increase, observations show more ice crystals and supercooled liquid droplets; such trends are not as evident in simulations.

1. Introduction

Clouds play a crucial role in influencing Earth's radiation budget (Liou, 1992). The cloud types, height, the partition of cloud phases, and microphysical properties of liquid droplets and ice crystals are important in determining the cloud radiative effect (Chen et al., 2000; Matus & L'Ecuyer, 2017).

Mixed phase clouds, clouds with the coexistence of liquid and ice, have been a focus of cloud microphysics research as many of their properties remain not fully understood (e.g., Korolev et al., 2017; Lohmann et al., 2016).

Project Administration: Minghui Diao
Resources: Ching An Yang, Minghui Diao
Supervision: Minghui Diao
Validation: Ching An Yang, Minghui Diao
Visualization: Ching An Yang, Minghui Diao
Writing – original draft: Ching An Yang, Minghui Diao
Writing – review & editing: Ching An Yang, Minghui Diao, Andrew Gettelman, Kai Zhang, Jian Sun, Greg McFarquhar

A frequently occurring process in mixed phase clouds, named the Wegener-Bergeron-Findeisen (WBF) process, describes ice crystal growth at the expense of liquid droplets as the liquid droplets evaporate to water vapor that deposits on ice crystals (Bergeron, 1928; Wegener, 1911). This occurs when ambient water vapor partial pressure (e) is lower than the saturation vapor pressure with respect to liquid ($e_{s,liq}$) but higher than the saturation vapor pressure with respect to ice ($e_{s,ice}$). The amount of ice and liquid and their mass partition in mixed phase clouds are crucial for determining cloud lifetime, radiative properties, and precipitation (e.g., Morrison et al., 2010; Mülmenstädt et al., 2015), as well as for developing model parameterizations that represent these properties (e.g., Tan & Storelvmo, 2016; Zhang et al., 2019).

Supercooled liquid water, that is, liquid droplets that exist below 0°C in both liquid and mixed phase clouds, was previously found to be underestimated in several global climate model (GCM) simulations, particularly over the Southern Ocean (Bodas-Salcedo et al., 2016; McCoy et al., 2016; Tan et al., 2016; Williams et al., 2013). Due to the scarcity of in situ observations in remote regions such as over the Southern Ocean, many evaluations of model biases rely on satellite observations (e.g., Kay et al., 2012; Trenberth & Fasullo, 2010). Guo et al. (2020), as an example, used satellite retrieval data from Cloud-Aerosol Lidar and Infrared Pathfinder Satellite Observation (CALIPSO) to compare with the Community Atmosphere Model version 5 (CAM5). They concluded that the model misclassifies liquid as ice, leading to an underestimation of liquid cloud occurrence frequencies and an overestimation of ice cloud occurrence frequencies in all vertical levels. The model also shows that the supercooled liquid fraction reaches 50% at −5°C, a much higher temperature than the observed temperature of −20°C where that fraction is reached. When comparing with airborne observations around Punta Arenas, Chile, D'Alessandro et al. (2019) showed that the CAM5 does not allow liquid and mixed phase clouds to exist at temperatures less than −15°C. The model was found to overestimate and underestimate liquid water content (LWC) in liquid and mixed phases, respectively, and underestimate ice water content (IWC) in ice and mixed phases, which demonstrates the importance of analyzing both occurrence frequencies and cloud water content of the three cloud phases. Another study compared ground-based observations of mixed phase clouds over the Arctic with the CAM5, and showed that revising the mixing volumes where supercooled liquid water and ice particles coexist in the model can reduce the effectiveness of the WBF process, which prolongs the lifetime of supercooled liquid water (Zhang et al., 2019). Klein et al. (2009) found an underestimation of the median liquid water path by a factor of three in single-column models and cloud-resolving models when comparing with the observations from the Mixed-Phase Arctic Cloud Experiment (M-PACE). That study emphasized the importance of ice microphysical processes, such as ice initiation and water vapor deposition rate on ice crystals, which contribute to the underestimation of the liquid water path.

Thermodynamic (i.e., temperature and relative humidity) and dynamic (i.e., wind speed and direction) conditions play an important role in the formation of mixed phase clouds. For example, using in situ aircraft observations over the Southern Ocean, D'Alessandro et al. (2019) showed increasing deviations of RH_{liq} from liquid saturation as ice mass fraction increases in the mixture of ice and liquid. Other studies also found that mixed phase clouds are influenced by vertical velocity (e.g., Bühl et al., 2019; Korolev & Field, 2008; Shupe et al., 2008) and horizontal wind direction (e.g., Gierens et al., 2020; Qiu et al., 2018) from the microscale to the mesoscale. Aerosol number concentration and size distribution are also known to influence the formation and evolution of ice particles and supercooled liquid water. Three hypothesized aerosol indirect effects for mixed phase clouds are: (a) the glaciation indirect effect, which describes increases of ice nucleating particles (INPs) that lead to more ice particles and ice phase precipitation (Lohmann, 2002); (b) the riming indirect effect, which describes increases of cloud condensation nuclei (CCN) concentrations that lead to smaller liquid droplets, less riming and smaller IWC (Borys et al., 2003); and (c) the thermodynamic indirect effect, which describes increases of CCN concentrations that lead to more liquid droplets, less secondary ice production (Hallett & Mossop, 1974) and fewer ice particles (Rangno & Hobbs, 2001). Using airborne observation data, Jackson et al. (2012) found a positive correlation between liquid number concentration inside clouds and aerosol number concentration below clouds. They also found a positive correlation between ice number concentration and aerosol number concentration above clouds. Storelvmo et al. (2011) conducted a modeling study for aerosol indirect effects on mixed phase clouds and found decreasing cloud lifetime due to increasing INP concentrations. They also found decreasing ice particle sizes and increasing cloud albedo due to increasing INP concentrations, similar to the Twomey effect on liquid clouds. These studies demonstrated the importance of thermodynamic conditions and aerosol indirect effects on cloud microphysical properties in the mixed phase cloud regime.

A recent campaign conducted in 2018 over the Southern Ocean, the Southern Ocean Clouds, Radiation, Aerosol Transport Experimental Study (SOCRATES; McFarquhar et al., 2021), has provided valuable airborne cloud observations for several scientific studies. For example, Wang et al. (2020) examined the importance of generating cells (GC) for producing mixed phase clouds over the Southern Ocean. They found enhanced IWC and LWC inside the GCs compared with the adjacent environment. D'Alessandro et al. (2021) showed that up to 70% of the supercooled liquid water and most of the spatially heterogeneous mixed-phase segments occurred between −20°C and 0°C. Zaremba et al. (2020) classified cloud top phases as a function of cloud top temperature using radar and lidar and concluded that liquid is the most dominant phase for cloud top. Another study by Gettelman et al. (2020) compared CAM6 simulations against SOCRATES observations and showed that CAM6 provides improved representations of supercooled liquid water and particle size distributions compared with CAM5. However, there is still a question that has not been addressed in these existing studies, that is, "how well do GCMs represent three cloud thermodynamic phases, cloud microphysical properties and aerosol indirect effects in the mixed-phase cloud regime between −40°C and 0°C over the Southern Ocean?"

This study examines ice particle and supercooled liquid water distributions over the Southern Ocean based on the SOCRATES. In situ observations are compared with simulations of three GCMs: the National Center for Atmospheric Research (NCAR) Community Atmosphere Model version 5 (CAM5) and version 6 (CAM6), and the Energy Exascale Earth System Model (E3SM) by the United States Department of Energy (DOE). CAM5 and CAM6 are the atmospheric component of the NCAR Community Earth System Model version 1 (CESM1) and version 2 (CESM2), respectively. Compared with CAM5, CAM6 has improvements applied to mixed phase cloud parameterization, prognostic precipitation species, and the interaction with aerosol schemes. E3SM uses a similar physics package as CAM6 but includes many differences, such as a different dynamical core, more vertical levels, a more detailed treatment of aerosol variety and properties, etc. The main goals of this work are to advance the understanding of statistical distributions of cloud phase and microphysical properties, the thermodynamic effect, and aerosol indirect effects on cloud characteristics over the Southern Ocean, as well as to provide evaluations on three model simulations.

In Section 2, the observation dataset and the set-up of model simulations are introduced. In Section 3, a case study of three cloud thermodynamic phases is presented. Their thermodynamic conditions (e.g., temperature and RH), cloud phases, and cloud microphysical properties are compared between the observations and model simulations. Statistical distributions of cloud phase occurrence frequencies, mass and number concentrations of cloud hydrometeors, effects of thermodynamic conditions, and aerosol indirect effects are also analyzed based on a synthesized observation dataset. Lastly, conclusions and implications are given in Section 4.

2. Instrumentations and Simulations

2.1. In Situ Airborne Observations

The SOCRATES campaign was a flight campaign funded by the U.S. National Science Foundation (NSF) and supported by NCAR (McFarquhar et al., 2021). The campaign was conducted between 62°S–42°S and 133°E–164°E over the Australasian section of the Southern Ocean region from 15 January to 24 February 2018. The SOCRATES campaign studied clouds, aerosols, cloud-aerosol interaction, precipitation, and radiation over the remote region of the Southern Ocean, where climate models tend to underestimate the shortwave radiation reflected by the low-level clouds in the Austral summer, especially in the colder sector of low-pressure systems. The research flights (RFs) targeted the cold dry sector of cyclones where the presence of strong westerly and southwesterly flows along with the cold ocean surface temperatures favor the formation of low-level and mid-level clouds such as stratocumulus. For this study, the analysis is restricted to data collected between −40°C and 0°C (also referred to as the mixed phase cloud regime hereafter), which allows for the presence of both supercooled liquid water and ice particles. A total of 15 RFs were conducted, and 111 total flight hours were flown during SOCRATES. Among these observations, 14 and 73 flight hours were at in-cloud and clear-sky conditions at −40°C–0°C, with average true airspeed at 156 and 178 m s^{-1}, respectively.

The NSF Gulfstream-V (GV) research aircraft was the platform used in the SOCRATES campaign, with scientific instruments installed to measure meteorological conditions, cloud hydrometeors, aerosol concentrations, and other quantities. A Rosemount temperature probe measured temperature, with an accuracy and precision of ±0.3 and 0.01 K, respectively. The Two-Dimensional Stereo Probe (2DS) and the cloud droplet probe (CDP) were
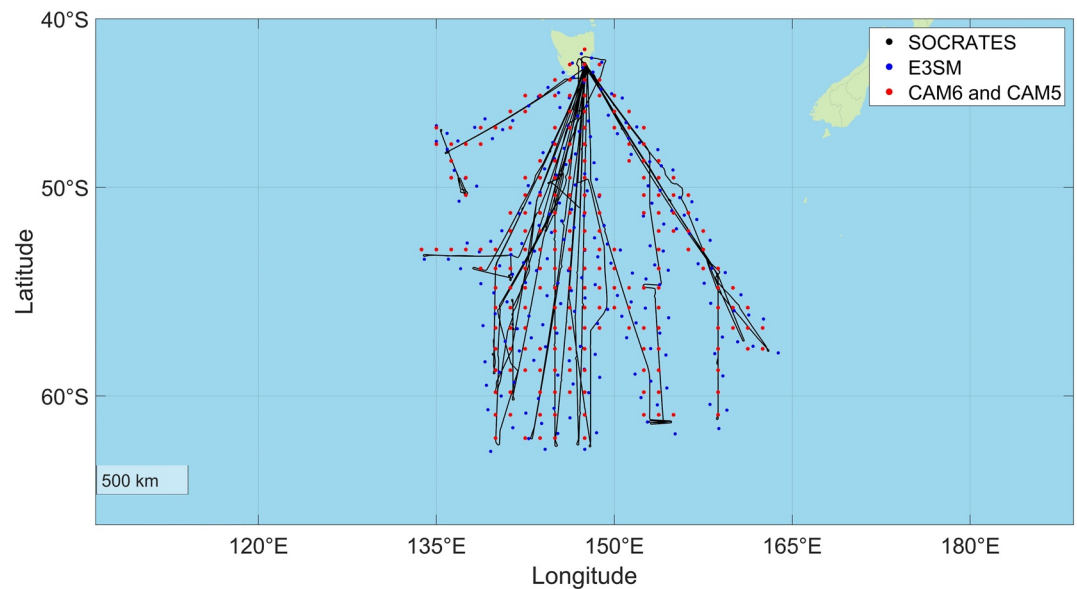
Figure 1. Flight tracks of a total 15 research flights in the NSF SOCRATES campaign (black) and the collocated grid coordinates for CAM6 (red), CAM5 (red), and E3SM (blue) simulations.

mounted underneath the aircraft wings to measure particle size distributions. The CDP measures particle sizes from 2 to 50 μm, with large uncertainties in measuring ice crystal size distributions due to potential shattering and their non-spherical nature (Hallett, 2004; McFarquhar et al., 2007). The 2DS uses two orthogonal laser beams that provide a high pixel resolution of 10 μm. It nominally measures particle sizes from 10 to 1,280 μm but has an uncertain depth of field for smaller particles (e.g., Baumgardner & Korolev, 1997), giving large uncertainties in calculated size distributions for size less than 50 μm (Jackson et al., 2012). Even though the width of the photodiode array for the 2DS probe is 1,280 μm, the sizes of larger particles whose center is in the photodiode array are estimated by fitting a circle around the visible part of the image and then using the diameter of the circle as the dimension. Thus, the range of 40–5,000 μm is used for 2DS measurement. The Ultra-High Sensitivity Aerosol Spectrometer (UHSAS) measures the number concentrations and size distributions of aerosols in the 60–1,000 nanometer (nm) size range. The particle sizes measured by UHSAS data may be underestimated compared with the real ambient aerosol sizes due to the sampling process that exposes particles to lower RH than the ambient. Another instrument, the Vertical Cavity Surface Emitting Laser (VCSEL) hygrometer, was mounted on top of the aircraft and reported water vapor molecule number density at 25-Hz resolution with an accuracy of ~6% and a precision of ≤1% (Zondlo et al., 2010). Its product of water vapor mixing ratio was reported in 1-Hz resolution, and a PI-calibrated dataset of water vapor mixing ratio is used in this study based on post-campaign laboratory calibration in summer 2018 (Diao, 2021). Water vapor and temperature data are used to calculate RH_{liq} and RH_{ice} by using the equations for $e_{s,liq}$ and $e_{s,ice}$ in Murphy and Koop (2005), respectively. Combining the uncertainties from water vapor and temperature measurements, the uncertainties for RH_{ice} are 6.9%–6.5%, and the uncertainties for RH_{liq} are 6.8%–6.4% from −40°C to 0°C, respectively. The Rosemount Icing Detector (RICE) measures supercooled water droplets by freezing the droplets collided with the detector and changing its constant vibration frequency. The data are, however, unavailable during the de-icing process and may not detect supercooled droplets for temperatures greater than −5°C. An estimated uncertainty in sensing the presence of LWC is at a limit of about 0.025 g m^{-3} (Mazin et al., 2001). The RICE is used as a supportive instrument in this study for cloud phase verification.

The observed cloud phases are determined based on the cloud phase identification method from Figure 1 of D'Alessandro et al. (2019). This method is optimized for the evaluation of GCMs with a consideration of the coarser grid-box scale and definitions of simulated cloud and aerosol properties. First, this method mainly uses optical array probes (OAP) to derive cloud phases and other microphysical properties (i.e., IWC, LWC, N_{ice}, and N_{liq}), which allows the simulated cloud properties to be truncated to the same size range as the OAP instruments. Second, this method uses a quantifiable threshold—ice mass fraction—to separate ice, mixed, liquid

phase, which can also be derived from the model output. These two main aspects differ from another cloud phase identification dataset for SOCRATES at 1-Hz resolution developed by D'Alessandro et al. (2021). That dataset uses LWC measured by King Probe in addition to the OAP measurements and defines a cloud segment to be mixed phase when both ice and liquid are observed, while the simulation cannot replicate the sensitivity of King probe and would contain coexisting ice and liquid in most cases at 100-km scale.

Measurements from CDP are categorized into three types (i.e., large aerosols, liquid droplets, and ice particles) based on various thresholds of particle number concentration (Nc_{CDP}) and mass concentration (Mc_{CDP}). That is, particles with either $Nc_{CDP} \leq 10^{-1.5}$ cm^{-3} or $Mc_{CDP} \leq 10^{-3.4}$ g m^{-3} are considered large aerosols; particles with $10^{-1.5} < Nc_{CDP} < 10^{-0.5}$ cm^{-3} and $Mc_{CDP} > 10^{-3.4}$ g m^{-3} are defined as ice particles; and particles with $Nc_{CDP} \geq 10^{-0.5}$ cm^{-3} and $Mc_{CDP} > 10^{-3.4}$ g m^{-3} are defined as liquid droplets. For the 2DS, if the ambient temperature $\geq -30°C$, particle number concentration (Nc_{2DS}), the maximum particle diameter (D_{max_2DS}), and the standard deviation of size distribution (σ_{D_2DS}) are used to categorize liquid droplets and ice particles. If the ambient temperature $< -30°C$, a check of CDP reading is also required. After identifying the phase for each cloud probe, LWC is calculated for all probes assuming spherical shape and liquid density of 1,000 kg m^{-3}. For the 2DS, IWC is calculated for the range of 40–5,000 µm following the habit-dependent mass-dimension (m-D) relationships documented in Wu and McFarquhar (2016). A crude estimate of spherical shape and ice density (900 kg m^{-3}) are used to derive IWC if CDP is identified as ice phase, which is subject to large uncertainty. But, the majority of CDP measurements (33,232 s) are identified as liquid phase, while only a small number of CDP measurements are identified as ice (690 s) and typically M_{CDP} is small for ice phase periods. The final cloud phase identification and cloud microphysical properties are based on a dataset that uses the combined measurements of 2DS and CDP to calculate the total IWC and LWC. Cloud phases are defined by using the mass fraction of ice (hereafter named as the glaciation ratio), that is, IWC/TWC, where TWC stands for total water content and equals the sum of LWC and IWC. Ice, mixed and liquid phases are defined when glaciation ratio >0.9, 0.1 ≤ glaciation ratio ≤ 0.9, and glaciation ratio <0.1, respectively (e.g., D'Alessandro et al., 2019; Korolev & Isaac, 2003).

The quality of this cloud phase identification method is further verified by comparing against the RICE detector and manually examining the cloud images from 2DS. In two scenarios, the cloud phases are revised manually after checking the cloud images. One scenario is that at temperatures less than $-25°C$, there are a few occasions (2386 s) where the cloud phase identification method using 2DS and CDP defines the clouds as liquid phase, yet the RICE detector shows no signal of supercooled liquid water, and the cloud images show ice particles. The other scenario is that at temperatures above 0°C, the method using 2DS and CDP identifies clouds as ice phase, yet the cloud images show drizzles (302 s). Besides these rare incidents, the automatic identification of the cloud phase compares well with the RICE detector.

2.2. Three GCM Simulations

This study evaluates three model simulations against the in situ observations, including the NCAR CESM1/CAM5 model, an updated version CESM2/CAM6 model, and the DOE E3SM/Atmosphere Model version 1 (EAMv1). Figure 1 shows the map of aircraft flight tracks and the collocated model output from three simulations.

Both CAM5 and CAM6 use a finite-volume dynamical core (Lin, 2004). The two models were run with a resolution of 0.9° × 1.25° and 32 vertical levels, a time step of 30 min, and were nudged toward MERRA-2 temperature and horizontal wind field reanalysis data. The model output was saved at the closest location to the aircraft flight track for every 1-min observation, which facilitates a more direct comparison between the simulations and observations. Both CAM5 and CAM6 were run with a spin-up time of one year and a relaxation time of 24 hr when nudged toward the reanalysis data. The CAM5 simulation uses the MG1 cloud microphysics scheme (Morrison & Gettelman, 2008) coupled with a modal aerosol module with three modes (MAM3; Liu et al., 2012). A detailed description of CAM5 was previously documented in Neale et al. (2012). The newer version, CAM6, uses the cloud microphysics scheme MG2 with additional improvements of ice nucleation, ice microphysics, prognostic precipitation species, and interaction with aerosol schemes to calculate cloud mass fractions and number concentrations (Gettelman & Morrison, 2015). The MG2 microphysics scheme is coupled with an updated modal aerosol module with four modes, MAM4 (Liu et al., 2016). The MAM4 has an additional aerosol mode named primary carbon compared with MAM3, improving aerosol resuspension, nucleation, scavenging, and sea spray emissions. CAM6 also uses Cloud Layers Unified By Binormals (CLUBB) for turbulence and shallow convection, which replaces the original shallow convection scheme in CAM5 (Park & Bretherton, 2009).

The DOE E3SM/EAM version 1, on the other hand, is a derivative of CAM6 with a spectral element dynamical core and modified physics parameterization schemes (Rasch et al., 2019). The vertical and horizontal resolutions of E3SM are 72 layers and 1° (such gridding resolution is named as ne30), respectively. A nudged simulation toward ERA5 temperature and horizontal wind was performed, with a relaxation time scale of 6 hr (Sun et al., 2019). The output closest to flight track location at a 1-min frequency is used for the comparison. The E3SM nudged simulation started on 1 December 2017 and was initialized with the initial condition output for December from a climatological run (for both atmosphere and land). This allows a relatively short simulation time for the model to spin up compared with using the default initial condition file. Similar to CAM6, E3SM also uses the MG2 microphysics scheme and MAM4, but with more detailed treatments of aerosol categories and processes such as light-absorbing particle deposition.

2.3. Approaches to Facilitate Comparisons Between Model Simulations and Observations

Due to differences of spatiotemporal resolutions and various definitions of cloud and aerosol variables between in situ observations and model simulations, several approaches are used to select collocated samples and recalculate model output variables for comparisons. First, for model output in an entire atmospheric column, only the model grid box with the closest location to the vertical location of the aircraft is selected. Second, since simulated cloud hydrometeors in the model cover the size range from zero to infinity, which exceeds the sampling range of CDP and 2DS, a size cutoff is applied to all simulated cloud properties by restricting the particle size to the range of 0–5,000 μm. As shown in the particle size distribution of simulated hydrometeors by Gettelman et al. (2020), simulated snow partially overlaps with the measurement range of combined 2DS + CDP. Therefore, the sum of simulated ice and snow mass concentrations for a specific size range (i.e., 0–5,000 μm in this study) is used to compare with the observed IWC derived from measurements of a similar size range. A similar method was previously used in several model-observation comparison studies, such as Fridlind et al. (2007), Eidhammer et al. (2014), and Patnaude et al. (2021). Table S1 in Supporting Information S1 shows the contributions of various discrete size ranges of ice and snow to their mass concentrations in the CAM6 simulation. The model output variables being processed for this partial size range include "LWC," "NUMLIQ," "IWC," "NUMICE," "AQSNOW," and "ANSNOW." These variables represent grid-average values for mass and number concentrations of liquid, ice, and snow, respectively. The simulated LWC and liquid number concentration (N_{liq}) are defined by the size-restricted "LWC" and "NUMLIQ," respectively. We further define the simulated IWC as the sum of size-restricted "IWC" and "AQSNOW" and the simulated ice number concentration (N_{ice}) as the sum of size-restricted "NUMICE" and "ANSNOW," which means that the simulated ice phase includes both ice crystals and snow since cloud measurements in the observations include both ice crystals and snow. Aerosol number concentrations (Na) from the simulations are also restricted to aerosol sizes ≤1,000 nm based on a log-normal distribution, which follows the size range of the UHSAS measurements. The RH_{ice} and RH_{liq} values in the simulations are calculated based on water vapor specific humidity and the saturation vapor pressure equations from Murphy and Koop (2005), which avoids using the RH variable directly reported by the model. The average values of calculated RH_{liq}, RH_{ice} in contrast to the original model output "RELHUM" in every 5°C temperature bin are shown in Figure S1 in Supporting Information S1. The simulated RH_{liq} shows the maximum values at 101%, 100%, and 105% for CAM6, CAM5, and E3SM, respectively. For the observations, RH_{liq} values greater than 105% are set as NAN values (processed for 2,019 s) due to the combined uncertainties from water vapor and temperature measurements.

The observations define in-cloud conditions as at least one cloud hydrometeor has been detected by either CDP or 2DS. The maximum and minimum LWC (IWC) values in the observations are 2.41 and 3.06×10^{-5} g m^{-3} (8.76 and 6.05×10^{-6} g m^{-3}), respectively. For simulations, if IWC or LWC is $<10^{-7}$ g m^{-3}, they are not considered as real hydrometeors and are set to zero. This means that for simulations, in-cloud conditions are defined as either IWC or LWC being $>10^{-7}$ g m^{-3}, while the remaining conditions are considered as clear sky. In addition, only N_{liq} and N_{ice} greater than 10^{-7} cm^{-3} are used in the analysis of simulations. These in-cloud thresholds are chosen mainly to facilitate the comparison between observations and simulations, since a higher threshold would significantly reduce the number of in-cloud samples from model output. Note that when LWC and IWC are below 0.001 g m^{-3}, the observations do not represent real clouds, but rather represent one or a few hydrometeors. For brevity, we call them in-cloud regions, but they differ from the conventional definition of clouds used in previous studies (e.g., McFarquhar et al., 2007; McFarquhar & Heymsfield, 2001). Table 1 summarizes the maximum and minimum values for thermodynamic conditions (i.e., temperature, pressure, RH_{ice}, and RH_{liq}) and cloud microphysical properties (i.e., LWC, IWC, N_{liq}, and N_{ice}) used for the analysis of observations and simulations.

Table 1
The Maximum and Minimum Values of Thermodynamic Conditions and Cloud Microphysical Properties Used in This Study for Observations and Simulations

Variables	1-s observations	200-s observations	580-s observations	CAM6	CAM5	E3SM
T (°C)	−39.7 to 0.0	−39.7 to 0.0	−39.7 to 0.0	−37.6 to 0.0	−37.4 to 0.0	−38.6 to 0.0
P (Pa)	37,623–96,848	37,644–97,131	37,645–96,958	32,207–96,777	32,212–98,315	31,915–99,664
LWC (g m⁻³)	3.06×10^{-5}–2.41	3.33×10^{-7}–0.74	1.20×10^{-7}–0.60	1.00×10^{-7}–0.36	1.02×10^{-7}–0.43	2.40×10^{-7}–0.40
IWC (g m⁻³)	6.05×10^{-6}–8.76	3.78×10^{-8}–0.89	1.30×10^{-8}–0.67	1.24×10^{-7}–0.17	1.20×10^{-7}–0.28	1.03×10^{-7}–0.18
N_{liq} (cm⁻³)	5.66×10^{-5}–565.72	2.96×10^{-7}–218.19	1.04×10^{-7}–210.79	4.04×10^{-7}–111.01	1.93×10^{-7}–150.09	1.36×10^{-7}–91.35
N_{ice} (cm⁻³)	5.66×10^{-5}–38.89	2.95×10^{-7}–4.34	1.04×10^{-7}–1.58	9.49×10^{-8}–0.09	1.77×10^{-7}–0.56	9.17×10^{-8}–2.49
In-cloud RH_{liq} (%)	2.6–105.0	3.8–103.1	6.0–101.7	18.0–101.3	42.3–99.5	17.9–104.5
In-cloud RH_{ice} (%)	2.9–146.7	4.1–140.3	7.3–131.7	19.5–133.8	52.1–115.8	19.1–143.8
Clear-sky RH_{liq} (%)	1.1–104.9	1.7–93.1	2.0–86.9	5.3–97.4	5.4–97.0	0.0–98.8
Clear-sky RH_{ice} (%)	1.2–142.2	2.1–117.7	2.3–109.2	6.3–110.9	6.5–103.6	0.0–125.0

To examine the effect of spatial scales to the comparison results, 1-Hz observations are averaged by various scales, including 200 s (i.e., 34.5 km horizontal resolution, since the average true airspeed of the aircraft at −40°C–0°C is 172 m s⁻¹) and 580 s (i.e., 100 km horizontal resolution) using a moving average method similar to D'Alessandro et al. (2019). A restriction on the averaging process of the observation data is added to reduce the impact of the saw-tooth data collection strategy during the SOCRATES campaign. Specifically, the observation data used to calculate the moving average surrounding each second must be within the pressure boundaries of one CAM model grid box. In addition, if more than 50% of the averaging data points are outside the pressure boundaries of such CAM model grid box, this averaged datum will be discarded and not used to compare with model output. This moving average generally leads to smaller values of average IWC, LWC, N_{ice}, and N_{liq} in coarser scale data than the 1-s data, since the coarser scale data include both clear-sky and in-cloud segments during the averaging process. Since these observation data represent averages over the entire length scale, they are comparable with simulated grid-average cloud quantities.

3. Results

3.1. Cloud Phases, Microphysical Properties, and Thermodynamic Conditions in a Case Study

A segment from the RF 05 was selected to show an example of supercooled liquid water and ice particle distributions using 2DS and CDP (Figure 2). The observed temperature ranges from −9°C to −6°C, and the RH_{liq} values are located around or slightly below liquid saturation between UTC 01:53:20 and 01:55:45, favoring the existence of supercooled liquid water at this period (Figure 2a). The magnitude of ice supersaturation (i.e., RH_{ice}—1) is about 5%–10%, which may partially contribute to the ice formations around UTC 01:56:00–01:56:40. The IWC values, derived from the combined 1-Hz CDP and 2DS measurements, remain relatively constant at 0.01 g m⁻³ for most in-cloud conditions, while the LWC are mostly above 0.1 g m⁻³ (Figure 2b). The cloud phase identifications are shown in Figure 2c. 2DS cloud imageries are shown in Figures 2d–2f for liquid, mixed, and ice phase, respectively. For this specific case, all three models simulate clouds for the entire period. Both CAM6 and E3SM show mixed phase clouds while CAM5 shows ice phase only.

3.2. Cloud Phase Occurrence Frequency and Distributions of LWC, IWC, and Glaciation Ratio

Cloud phase occurrence frequencies for the entire SOCRATES campaign are compared with model simulations (Figure 3). The number of samples for three cloud phases is shown in Figure S2 in Supporting Information S1. Figures 3b and 3c show the cloud phase occurrence frequencies for 200 and 580 s spatially averaged observation (horizontal scales of 35 and 100 km, respectively). An increase in spatial scale also increases the occurrence frequencies of mixed phase between −35°C and 0°C by a factor of 2–4, that is, mixed phase frequencies are 0.05–0.1 for 1-s observations, compared with 0.1–0.2 for 200 s and 0.1–0.35 for 580-s observations.
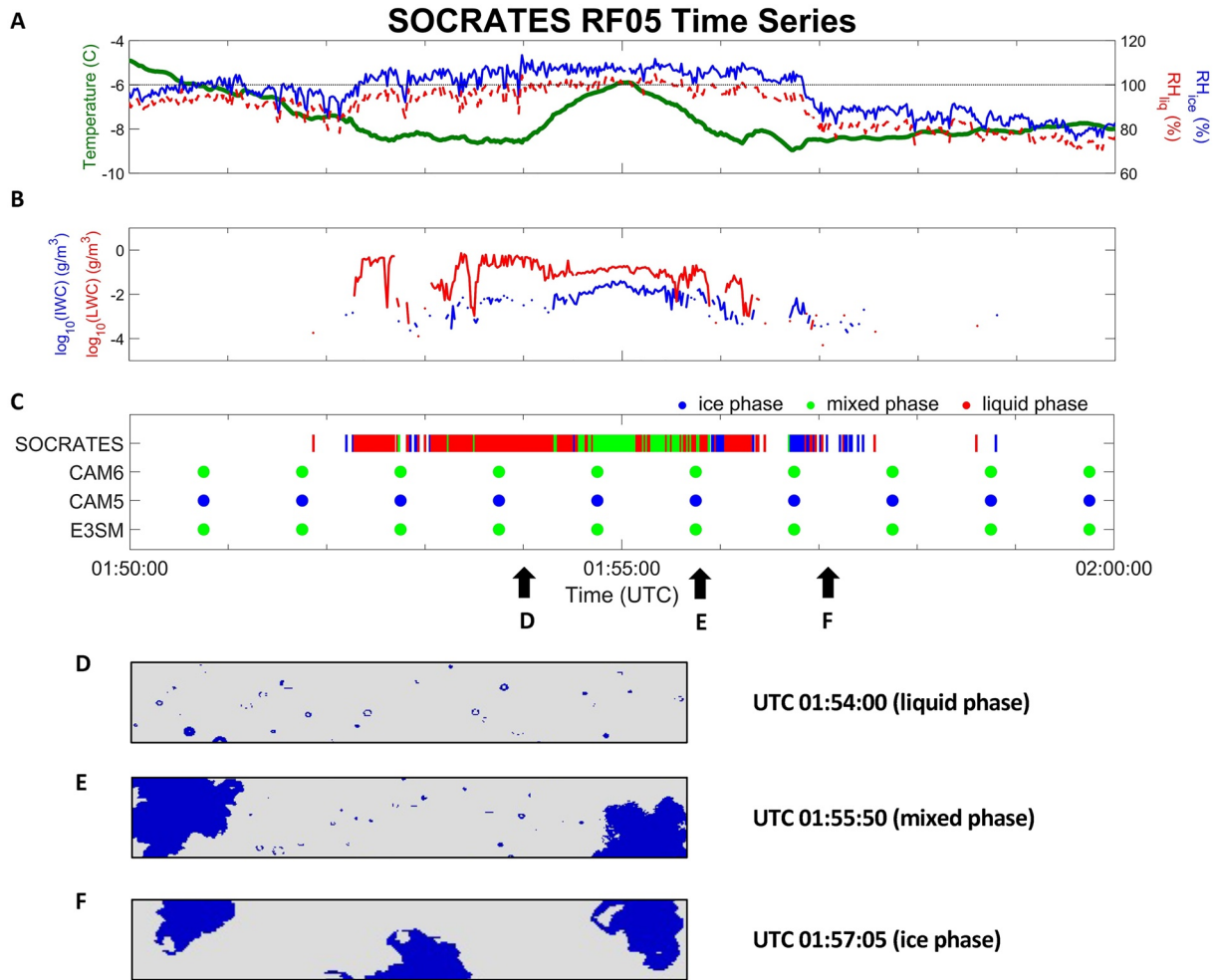
Figure 2. An example time series of clouds with a mixture of ice, liquid, and mixed phases in NSF SOCRATES campaign Research Flight 5 (RF05). (a) 1-Hz observations of temperature (dark green), RH_{ice} (blue), RH_{liq} (red), and RH = 100% (dashed black). (b) 1-Hz observations of log-scale IWC (blue) and LWC (red) using 2DS and CDP probes. (c) Cloud phases identified from the observations (vertical bars) and the models (dots). (d–f) illustrate the seconds of liquid, mixed, and ice cloud particle imageries, respectively, captured by the 2DS.

Simulations are further examined with two types of simulated IWC–one contains both ice crystals and snow (Figures 3d–3f) which is used as the default definition of simulated IWC, while the other contains only ice crystals (Figures 3g–3i). Excluding snow as part of the simulated IWC increases (decreases) liquid (mixed) phase frequency by 0.1–0.2 in three simulations. Compared with the 580-s observations, CAM6 (Figure 3d) shows the most similar cloud phase frequencies for ice, liquid, and mixed phases among the three models. The 580-s averaged observations show an intersection of the liquid (red) and ice (blue) frequency lines with a significant decrease (increase) in ice (liquid) phase frequency between −20°C and −15°C. A similar feature is shown in CAM6 but occurs at a higher temperature range between −15°C and −10°C. The minor issue with CAM6 is the slightly lower liquid and mixed phase frequency and higher ice phase frequency by 0.1 at −10°C to −5°C than 580-s averaged observations. CAM6 significantly improves the presence of supercooled liquid water below −10°C compared with CAM5, since CAM5 shows zero frequency of liquid-containing clouds below −10°C. The lack of supercooled liquid water at temperatures less than −15°C in CAM5 was also shown in the previous work of D'Alessandro et al. (2019). E3SM (Figure 3f) underestimates (overestimates) the frequency of ice phase clouds below (above) −20°C by 0.1–0.3 compared with 580-s averaged observations. E3SM was found to overestimate of liquid cloud fraction between −20°C and −30°C at high latitudes (Zhang et al., 2019). It was also found to underestimate pure ice clouds at most temperatures except for close to −40°C based on a global-scale evaluation (Rasch et al., 2019). A similar result of E3SM overestimating supercooled liquid water below −20°C was also documented in Zhang et al. (2020) for an analysis of Arctic clouds. The similarity of E3SM model biases between
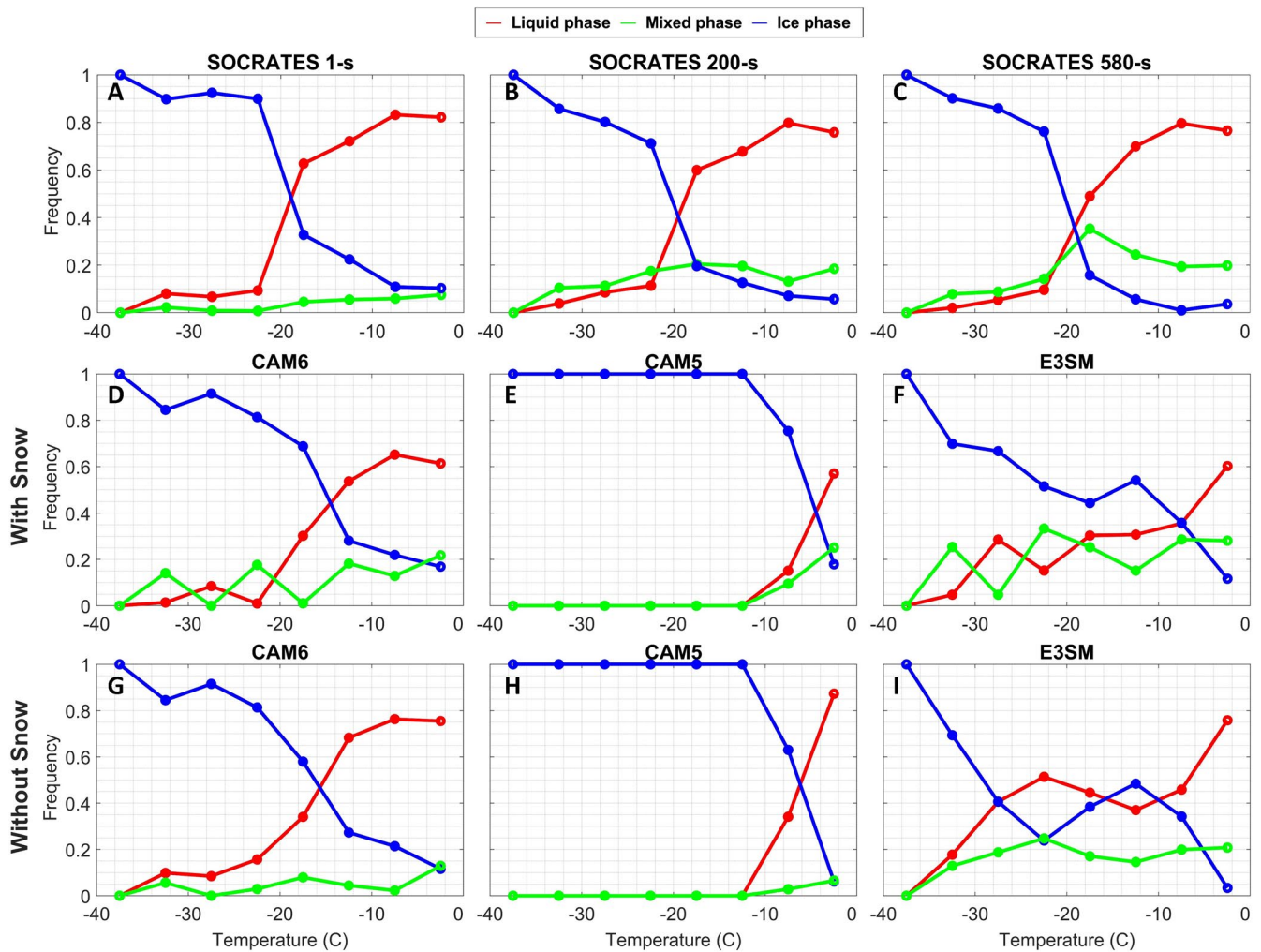
Figure 3. Cloud phase occurrence frequencies for (a) 1-Hz SOCRATES observations, (b) 200-s averaged observations, and (c) 580-s averaged observations with temperature ranged from −40°C to 0°C, binned by 5°C. Cloud phase occurrence frequencies for CAM6, CAM5, and E3SM are shown for two types of simulated IWC: (d–f) including snow and (g–i) excluding snow. Liquid, mixed, and ice phase are denoted by red, green, and blue colors, respectively.

those previous studies and this study suggests that these model biases of cloud phase frequency are consistently shown for high latitudinal regions in both hemispheres. Yet more detailed hemispheric comparisons are needed in future work.

Given the importance of temperature nudging on simulation results (e.g., Gettelman et al., 2020), Figure S3 in Supporting Information S1 compares the temperatures of CAM6, CAM5, and E3SM simulations with observations using the nearest model grid to the flight track. In general, both CAM5 and CAM6 show distributions of temperature biases skewed toward low biases, while E3SM shows a more symmetrical temperature bias distribution as well as a smaller mean bias compared with the observations. That is, 65% of E3SM temperatures are within 1 degree of the observed temperatures (Figure S3a in Supporting Information S1). This is mainly due to different reanalysis data used for nudging, that is, E3SM was nudged toward ERA5 data while CAM6 and CAM5 were nudged toward MERRA-2. All three models show similar temperature vertical profiles with respect to pressure compared with the observations (Figure S3b in Supporting Information S1). This analysis demonstrates that CAM6 having the most similar cloud phase frequency distributions to the observations cannot be explained by a closer temperature match to the observations, since E3SM shows the most similar temperature distribution to the observations.

In addition, the impacts of various in-cloud condition thresholds on cloud phase statistical distributions are also examined in Figure 4. Number of samples for Figure 4 is shown in Figure S4 in Supporting Information S1.
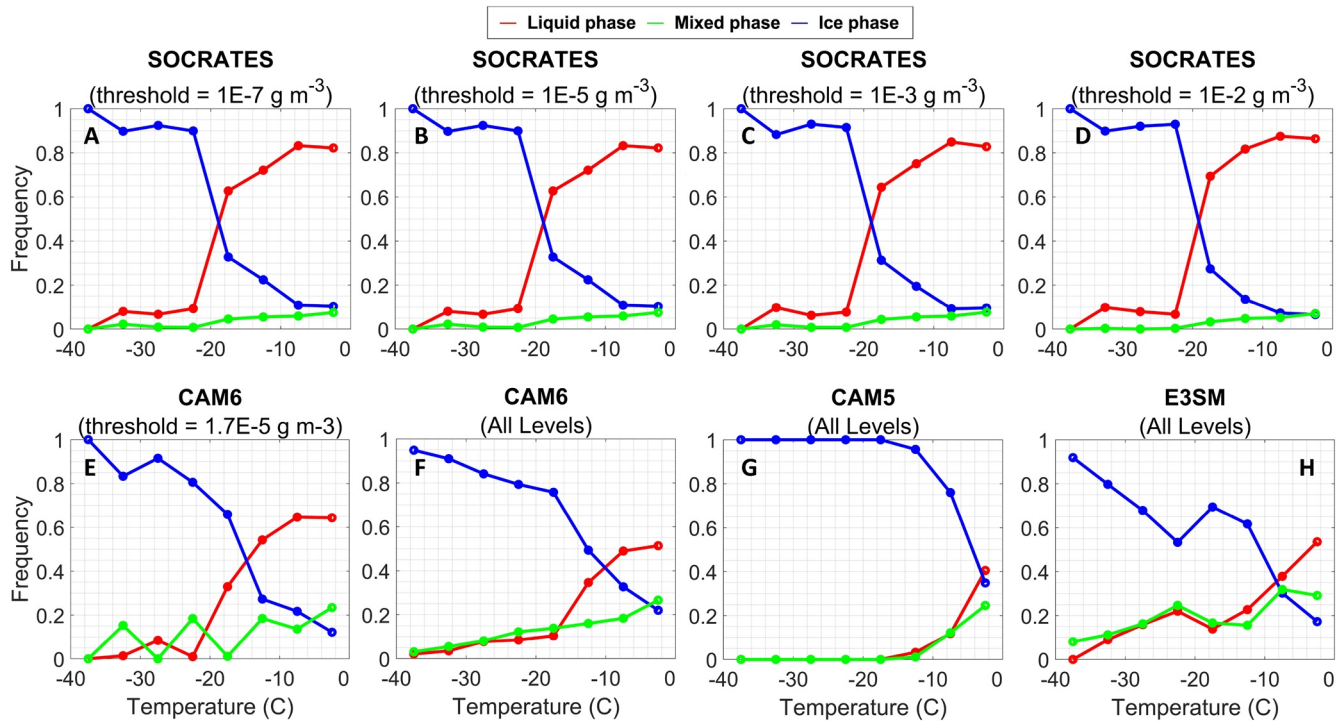
Figure 4. Sensitivity tests on cloud phase occurrence frequencies using various thresholds for defining in-cloud conditions for SOCRATES observations, including (a) 10^{-7} g m^{-3}, (b) 10^{-5} g m^{-3}, (c) 0.001 g m^{-3}, and (d) 0.01 g m^{-3}. (e) CAM6 simulation using in-cloud threshold of 1.7×10^{-5} g m^{-3}. Using all model output in the entire temperature range of −40°C to 0°C for (f) CAM6, (g) CAM5, and (h) E3SM.

Figures 4a–4d compare various in-cloud thresholds: 1×10^{-7}, 1×10^{-5}, 0.001, and 0.01 g m^{-3}. All of these sensitivity tests show very consistent results even when different in-cloud thresholds are used. In addition, using a higher in-cloud threshold (i.e., 1.7×10^{-5} g m^{-3}) for the CAM6 simulation (Figure 4e) also shows similar results of cloud phase frequency distribution compared with using the threshold of 1×10^{-7} g m^{-3}. Another sensitivity test in Figures 4f and 4h uses the entire model columns between −40°C and 0°C to compare with observations, in contrast to the restriction of comparing observations with the nearest model grid box only in vertical level (as shown in Figures 2, 3, and 5–14). The result shows that removing the temperature collocation restriction worsens the model-observation comparison results. Nevertheless, the main conclusions are consistently seen. For example, CAM6 still shows the most comparable results to observations, while E3SM still underestimates and overestimates ice phase below −20°C and above −20°C, respectively. This sensitivity test suggests that the model biases seen in this study are unlikely driven solely by the mismatches of time and space for simulated and observed cloud occurrences.

Effects of spatial scales are examined in Figures 5a–5c for observations that are spatially averaged by every 10, 50, 100, 200, 290, and 580 s, which represent horizontal scales of 1.7, 8.6, 17, 35, 50, and 100 km, respectively. The overall trend of an increasing liquid (ice) phase frequency in a warmer (colder) environment remains unchanged. Larger spatial scales consistently show increases in the occurrence frequencies of mixed phase between −35°C and 0°C. Furthermore, length scales of three cloud phases in 1-Hz observations are examined in Figures 5d–5f. The number of samples for Figure 5 is shown in Figure S5 in Supporting Information S1. Length scales of individual cloud phase segments are calculated by the consecutive seconds of the same cloud phase in 1-Hz observations. The shorter and longer length scales represent more heterogeneous and homogeneous distributions of cloud phases, respectively. The observations show more mixed phase segments at shorter length scales (1–3 s) than longer length scales (>10 s), while the liquid and ice phases dominate the longer length scales (>10 s). This result indicates that the coexistence of ice and liquid occurs more frequently at shorter length scales, likely due to the effective transition from liquid to ice via the WBF process.

Cloud microphysical properties, that is, LWC, IWC, and glaciation ratios, are examined for various temperatures (binned by 5°C) in Figure 6. The number of samples for this analysis is shown in Figure S6 in
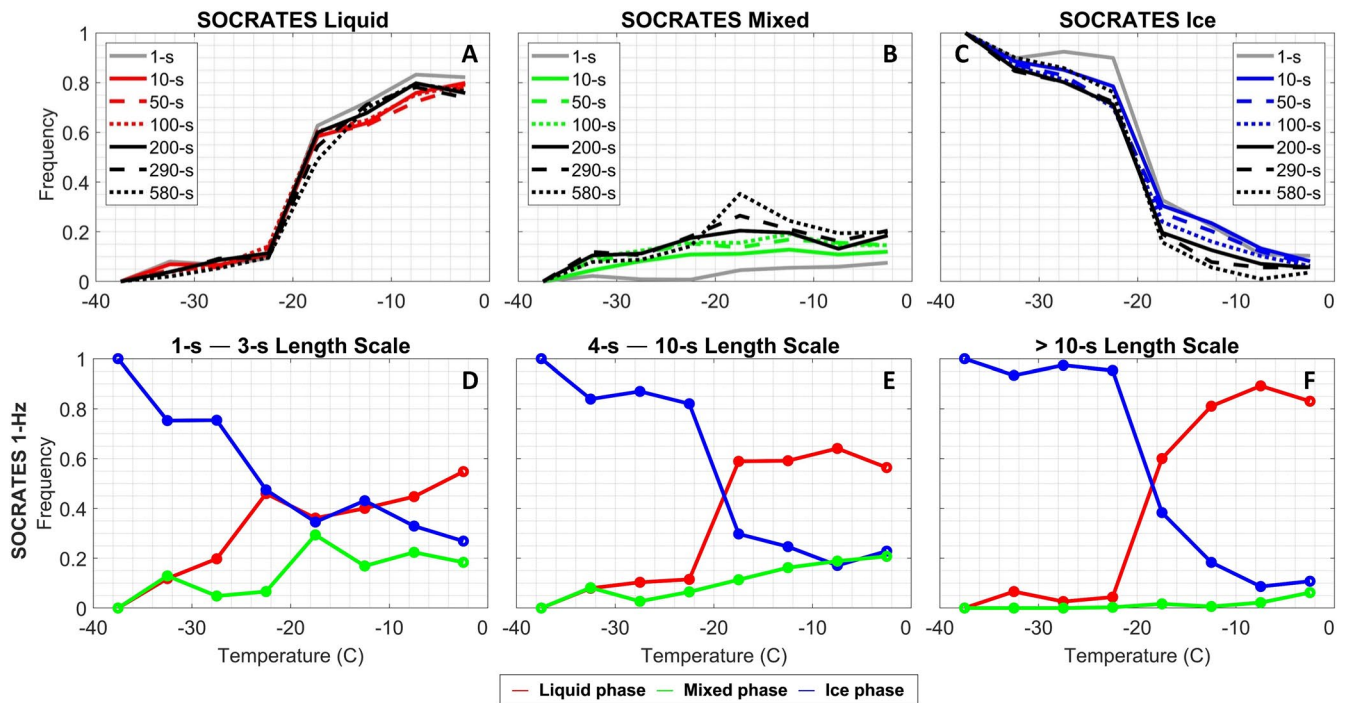
Figure 5. Cloud phase occurrence frequencies for (a) liquid phase, (b) mixed phase, and (c) ice phase are shown for 1-, 10-, 50-, 100-, 200-, 290-, and 580-s averaged observations. (d–f) Occurrence frequency of various length scales of cloud phase, calculated based on 1-Hz observations, including (d) 1–3 s length scale, (e) 4–10 s length scale, and (f) more than 10 s length scale.

Supporting Information S1. About 1-, 200-, and 580-s averaged observations are compared with model simulations. At temperature greater than −35°C, averaging observations over 200 s significantly reduces the average LWC and IWC by 1–2 orders of magnitude than the 1-s data, while the 580-s averaged observations show a further reduction of LWC and IWC by up to 0.5 order of magnitude. The moving averages generally lead to smaller values of average IWC, LWC, N_{ice}, and N_{liq} in coarser scale data compared with the 1-s data, since the coarser scale data include both clear-sky and in-cloud segments during the averaging process. Compared with 580-s averaged observations, CAM6 (E3SM) shows similar average LWC to the observations above −25°C (−20°C) but higher average LWC at lower temperatures by 1–2 orders of magnitude. Consistent with Figure 3, CAM5 lacks LWC at temperatures less than −10°C. For the average IWC, CAM6 underestimates IWC by 0.5–1 order of magnitude between −40°C and −30°C compared with 580-s averaged observations. E3SM underestimates IWC by 0.5–1 order of magnitude between −40°C and −20°C, and overestimates IWC by 0.5–1 orders of magnitude between −20°C and 0°C.

Two types of glaciation ratios are calculated. One is for all in-cloud conditions (Figures 6g–6i), and the other one is for conditions with coexisting ice particles and supercooled liquid water only (Figures 6j–6l). For the former type, the glaciation ratios are controlled by the ratios between ice phase and liquid phase occurrence frequencies, the two dominant phases. For the latter type, the glaciation ratios are controlled by the mass partitioning between ice and liquid when they coexist. For the former type of glaciation ratios, CAM6 shows the most similar results to the 580-s averaged observations (Figure 6g), which is consistent with the cloud phase frequency analysis in Figure 3. The latter glaciation ratios in CAM6 (Figure 6j) are close to the averaged observations above −20°C but are significantly lower by 0.2–0.6 below −20°C compared with observations due to the underestimation of IWC. This result is consistent with the LWC and IWC analysis shown in Figures 6a and 6d. E3SM overestimates the former type of glaciation ratios above −20°C and underestimates both the former and the latter type of glaciation ratios below −20°C. These analyses show that the underestimation of IWC and overestimation of LWC by CAM6 and E3SM at temperatures below −20°C leads to large biases of mass partitioning inside the mixture of ice and liquid.

A similar analysis to Figure 6 is done using simulated IWC containing only ice crystals (Figure S7 in Supporting Information S1). When excluding snow in the simulated IWC, larger model biases of IWC by a factor of
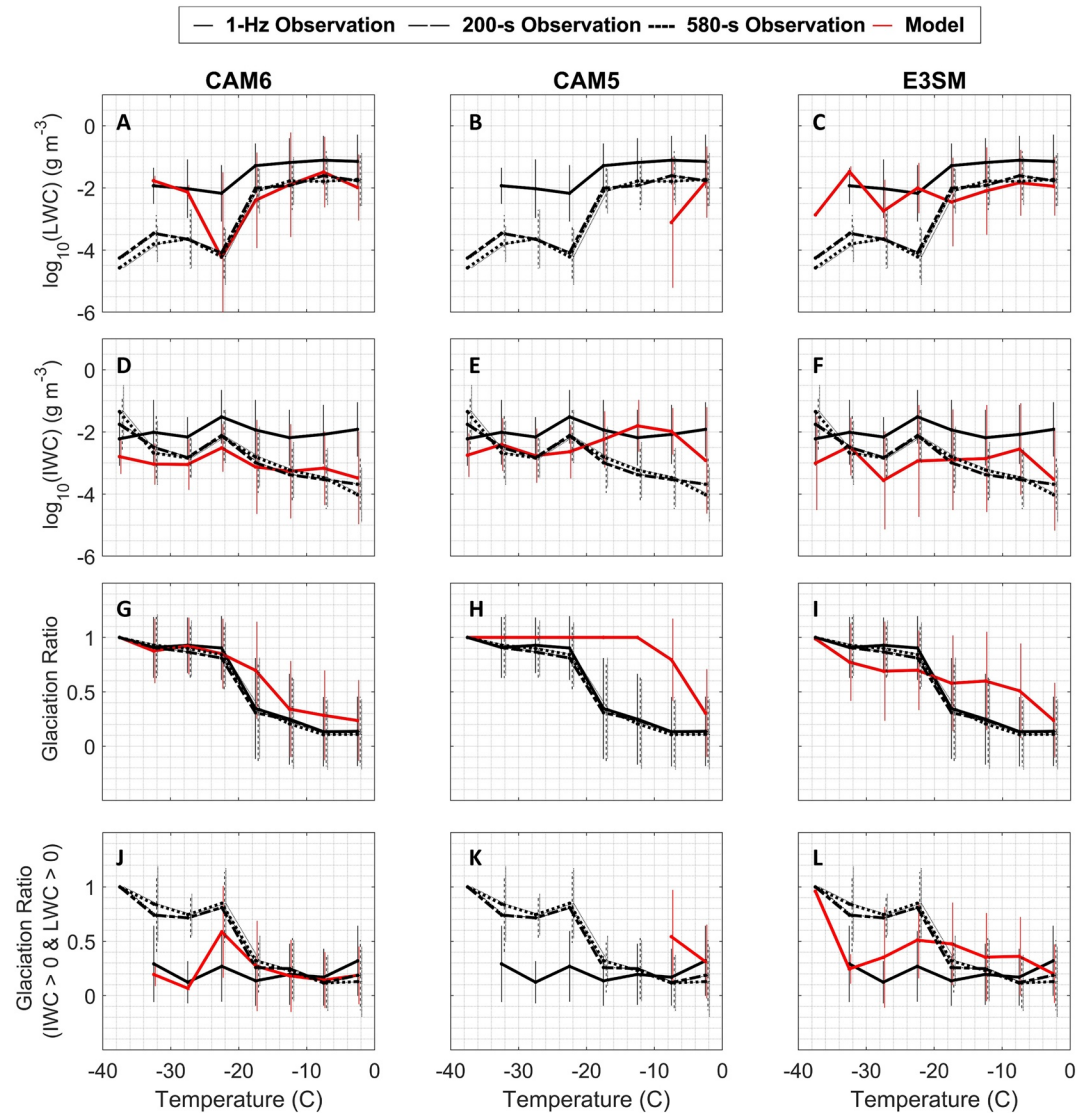
Figure 6. Averages and standard deviations of (a–c) log-scale LWC, (d–f) log-scale IWC, (g–i) glaciation ratio (i.e., IWC/TWC), and (j–l) glaciation ratio only when ice particles and supercooled liquid water coexist (i.e., IWC/TWC only when both IWC > 0 and LWC > 0). 1-Hz observations (solid black), 200-s observations (dashed black), 580-s observations (dotted black), and model simulations (red) are binned at 5°C interval from −40°C to 0°C.

0.5–1 are seen compared with including snow in the simulated IWC. Additionally, a sensitivity test is conducted to examine the impacts of model output frequency, by using E3SM output closest to every 1 s, 1 min, and 10 min of observations (Figure S8 in Supporting Information S1). Increasing the temporal resolution also increases the liquid and mixed phase frequencies. Overall, the analysis shows very similar results for average LWC, IWC, and glaciation ratios at various temperatures regardless of using various model output frequencies.

3.3. Thermodynamic Conditions for Clear-Sky, In-Cloud Conditions, and Three Cloud Phases

Thermodynamic conditions are crucial for the formation of ice particles and supercooled liquid water, as illustrated in the case study in Section 3.1. Figure 7 shows probability density functions (PDFs) of temperature and RH_{ice} categorized by in-cloud and clear-sky conditions (top two rows) and three cloud phases (bottom two rows). The PDF is calculated as the number of samples of a certain condition (such as in-cloud) at each bin divided by the total number of samples of that condition in all bins.
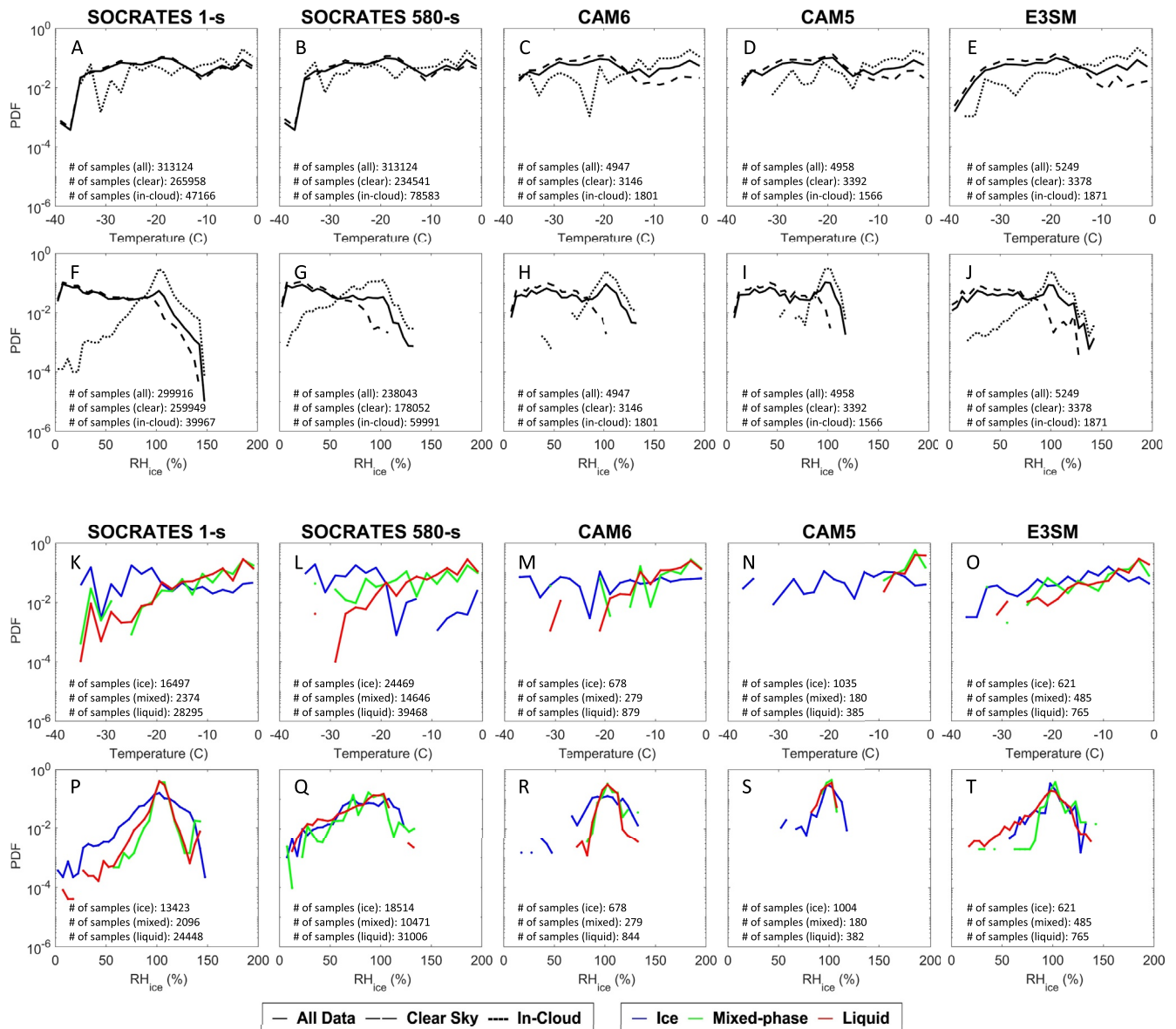
Figure 7. PDFs of (a–e) temperature and (f–j) RH_{ice} for all data (solid black line), clear-sky (dashed black), and in-cloud (dotted black) conditions. PDFs of (k–o) temperature and (p–t) RH_{ice} separated into three cloud phases, that is, ice (blue), mixed (green), and liquid (red) phase. Each PDF is calculated by the number of a certain condition in a bin divided by the total number of samples of that condition of all bins.

PDFs of temperatures of both clear-sky and in-cloud conditions are comparable between observations and simulations. Specifically, all three models show higher (lower) PDFs of in-cloud condition compared with the PDFs of clear-sky condition at temperatures above (below) $-15°C$, which is consistent with the distributions seen in the 1- and 580-s observations. This feature indicates that the general vertical locations of cloud layers are similar between the observations and model simulations.

PDFs of RH_{ice} for in-cloud conditions in the simulations show lower maximum values (CAM6 134%, CAM5 116%, and E3SM 144%) compared with 1-s observations (147%), but the simulated values of CAM6 and CAM5 are closer to 580-s averaged observations (132%). Similarly, PDFs of RH_{ice} for clear-sky conditions in the simulations show lower maximum values (CAM6 111%, CAM5 104%, and E3SM 125%) than 1-s observations (142%) but are closer to 580-s averaged observations (109%). The simulations also underestimate the frequencies of sub-saturated conditions for in-cloud RH_{ice}, since the 1- and 580-s averaged observations show minimum in-cloud RH_{ice} at 3% and 7%, respectively, while simulations show minimum values of 19%–52%.
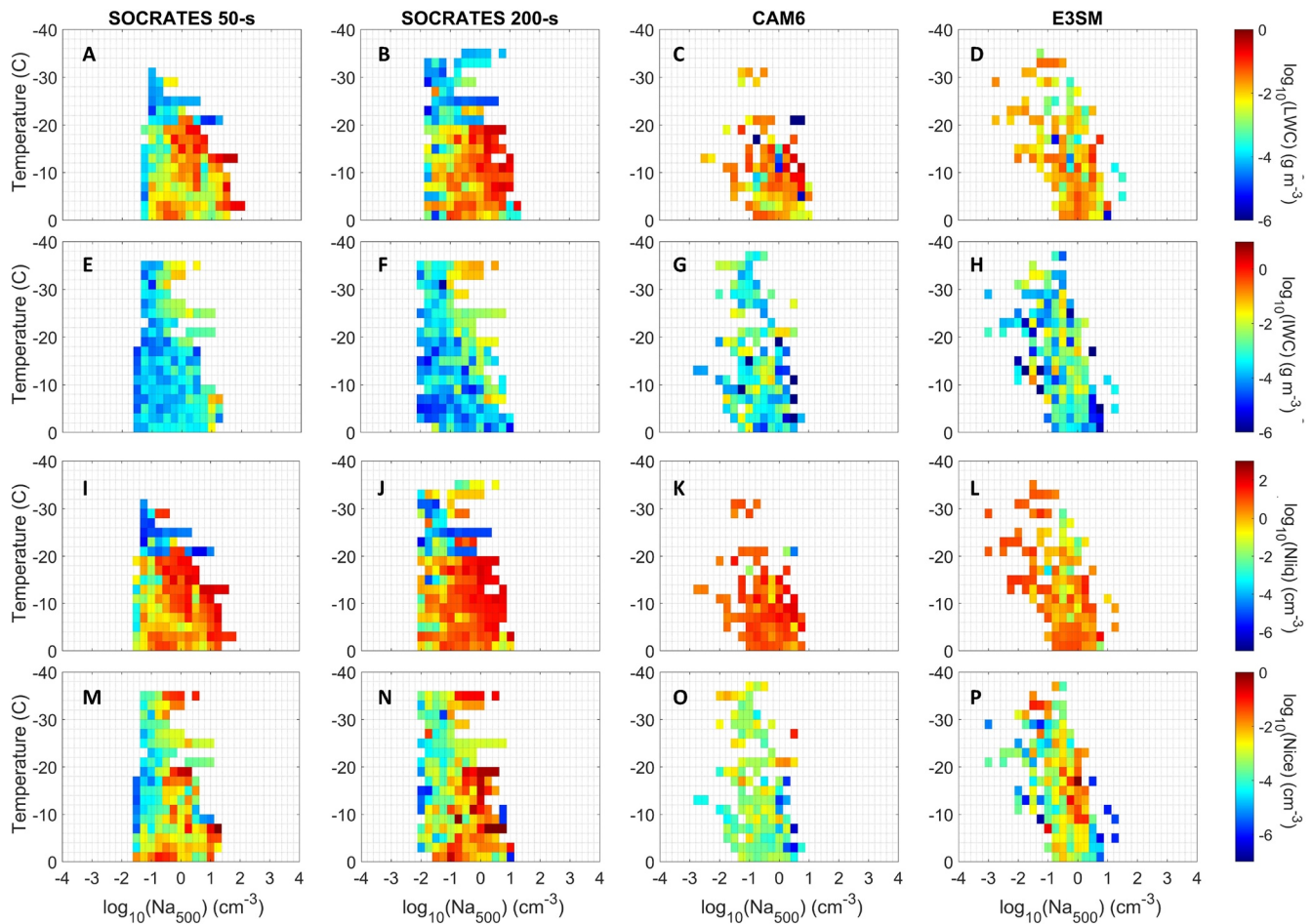
Figure 8. Cloud microphysical properties with respect to logarithmic scale Na_{500} for 1-s observations, 580-s averaged observations, CAM6, and E3SM at various temperatures. Bin colors denote the average of (a–d) $\log_{10}(LWC)$, (e–h) $\log_{10}(IWC)$, (i–l) $\log_{10}(N_{liq})$, and (m–p) $\log_{10}(N_{ice})$.

In terms of PDFs of RH_{ice} in three cloud phases, the peak positions of RH_{ice} in 1-s observations are located around 100%−102% for all three phases. For 580-s observations, the frequencies are similar between the peak position at 102% and the surrounding values from ~85% to 100% due to the inclusion of clear-sky segments in the averaging process. Three simulations show peaks of in-cloud RH_{ice} around 100% but with narrower ranges for all three cloud phases. For both observations and simulations, mixed phase is associated with a narrower RH_{ice} range than ice and liquid phases, consistent with the theoretical condition for WBF process with $e_{s,ice} < e < e_{s,liq}$. The lack of sub-saturated conditions for ice phase may contribute to the underestimation of ice growth and the riming effect during sedimentation, which possibly leads to lower IWC in the simulations.

3.4. Aerosol Indirect Effects on Cloud Microphysical Properties

In this section, aerosol indirect effects on cloud microphysical properties at various temperatures are examined based on the relationships between total aerosol number concentrations (Na) and cloud microphysical properties (Figures 8–11). According to previous studies using in situ measurements to examine aerosol indirect effects (e.g., Chubb et al., 2016; Field et al., 2012; Wood et al., 2018), aerosol number concentrations were often restricted to clear-sky conditions for the analysis of relationships between aerosols and cloud properties in order to reduce the impacts of cloud hydrometeors on aerosol measurements. Thus, average aerosol number concentrations were calculated using clear-sky segments only for 50-s averaged and 200-s averaged observations. Considering that simulated aerosol number concentrations represent the aerosol concentrations in a model grid box, the observed aerosol concentrations are not restricted to only above or below clouds in this analysis as commonly done for process orientated studies. In addition, since CAM5 significantly underestimates the amount of supercooled
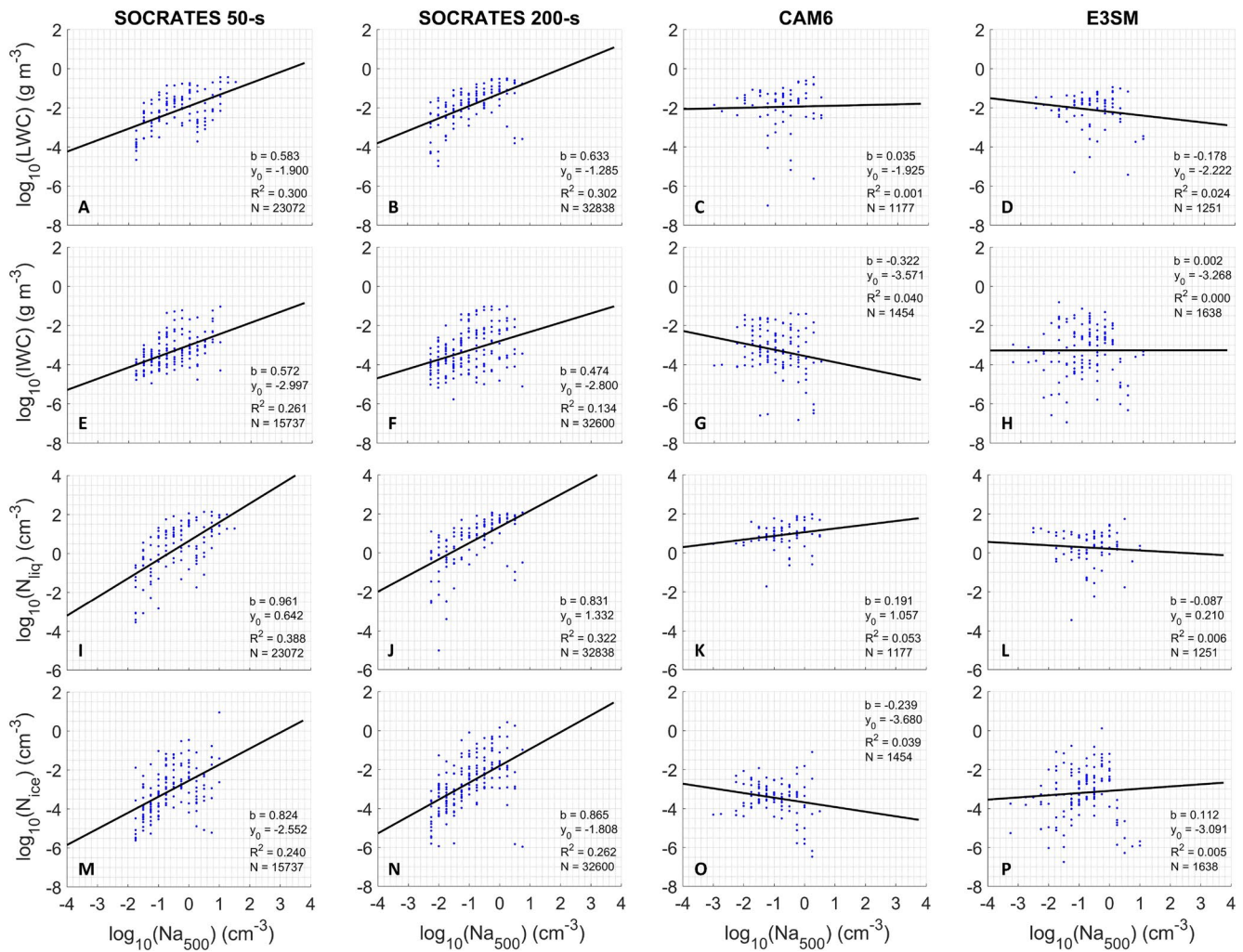
Figure 9. Linear regressions applied (black line) for the bin-average of (a–d) LWC, (e–h) IWC, (i–l) N_{liq}, and (m–p) N_{ice} in relation to $log_{10}(Na_{500})$. Bin sizes follow the respective sub-panels in Figure 8. The slope, intercept, R^2 values, and number of samples are shown in the text box. The analyses of LWC and N_{liq} are restricted to −20°C–0°C. The analyses of IWC and N_{ice} are restricted to −36°C–0°C.

liquid water below −10°C, the model evaluation in this section focuses on CAM6 and E3SM only. The analysis is based on Na separated into two groups—aerosols with diameters >500 nm (hereafter named as Na_{500}) and diameters > 100 nm (named as Na_{100}). Figures S9 and S10 in Supporting Information S1 show the number of samples used for the analysis of Na_{500} and Na_{100}, respectively. Previously, DeMott et al. (2010) showed that at temperatures higher than −36°C, Na_{500} is well correlated with the number concentrations of INPs, which can facilitate ice crystal formation during heterogeneous nucleation.

For the impacts of larger aerosols, as $log_{10}(Na_{500})$ increases, the 50- and 200-s averaged observations both show increasing $log_{10}(LWC)$ and $log_{10}(N_{liq})$ between −20°C and 0°C and increasing IWC and N_{ice} between −36°C and 0°C (Figure 8). Aerosol indirect effects are further quantified by applying linear regressions to cloud microphysical properties in relation to $log_{10}(Na_{500})$ (Figure 9). The linear regression analysis in Figure 9 examines the bin-average $log_{10}(LWC)$ and $log_{10}(N_{liq})$ between −20°C and 0°C, as well as the bin-average IWC and N_{ice} between −36°C and 0°C, since these two temperature ranges show distinct aerosol indirect effects (Figure 8). The slopes (b) of the linear regressions for logarithmic scale LWC, IWC, N_{liq}, and N_{ice} in 50-s (200-s) observations are 0.58, 0.57, 0.96, and 0.82 (0.63, 0.47, 0.83, and 0.87), respectively. The similar slopes between LWC and IWC as well as between N_{liq} and N_{ice} indicate that Na_{500} has similar magnitudes of impacts on liquid droplets and ice particles.
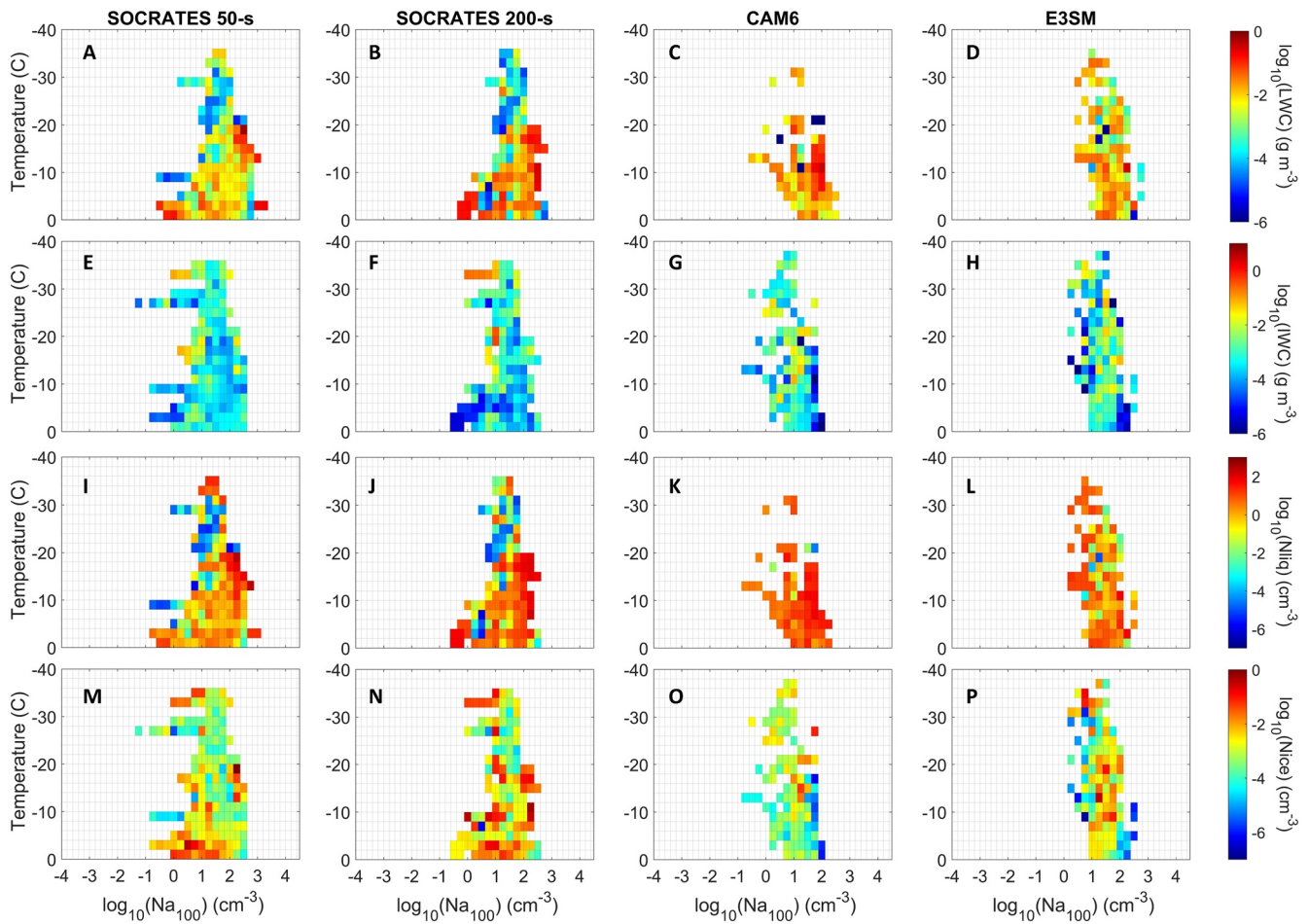
Figure 10. Similar to Figure 8 but for the relationship with $\log_{10}(Na_{100})$.

For the impacts of smaller aerosols (Figures 10 and 11), Na_{100} shows similar magnitude of impacts on N_{liq} ($b = 0.81$, 0.63) compared with Na_{500} (0.96, 0.83), but much smaller impacts on LWC (0.23, 0.18) compared with Na_{500} (0.58, 0.63) for 50- and 200-s observations, respectively. No significant correlation is seen between IWC and Na_{100}. These results indicate that both larger and smaller aerosols may serve as CCN to facilitate liquid droplet formation, while larger aerosols more likely exceed the critical radius for spontaneous droplet formation. The lack of impacts from Na_{100} on ice phase is consistent with the fact that larger aerosols are more likely to be activated as INPs. Overall, these results indicate Twomey effects from larger aerosols on both liquid droplets and ice particles in the mixed-phase cloud regime, but smaller aerosols only show Twomey effect on liquid droplets. When smaller aerosols act as CCN, the riming indirect effect and the thermodynamic indirect effect can both lead to higher N_{liq}, which further lead to smaller IWC via less effective riming and less effective secondary ice production, respectively. However, the thermodynamic indirect effect would also lead to smaller N_{ice}, while the riming indirect effect has a smaller impact on N_{ice}. Since Figures 11m shows no significant change of N_{ice} with respect to increasing Na_{100}, it indicates that the riming indirect effect is the dominant mechanism seen for indirect effect from small aerosols while the thermodynamic indirect effect is less dominant over the Southern Ocean. On the other hand, the glaciation indirect effect seems to be the dominant indirect effect from larger aerosols, since larger aerosols acting as INPs can lead to higher N_{ice} and higher IWC, which is consistent with Figures 9e and 9m. In terms of model simulations, both CAM6 and E3SM capture the decreasing trend of maximum Na_{500} and Na_{100} as temperature decreases. Yet, the maximum values of simulated Na_{500} and Na_{100} are 10 and 100 cm^{-3}, respectively, which are 0.5–1 order of magnitude smaller than the 200-s observations (Figures 8 and 10). For aerosol indirect effects of Na_{500}, CAM6 shows small positive correlations with N_{liq} ($b = 0.19$), negative correlations with IWC (-0.32) and N_{ice} (-0.24), and no significant correlations with LWC (Figure 9). E3SM shows small negative correlations with LWC ($b = -0.18$), N_{liq} (-0.087), and small positive correlations with N_{ice} (0.11).
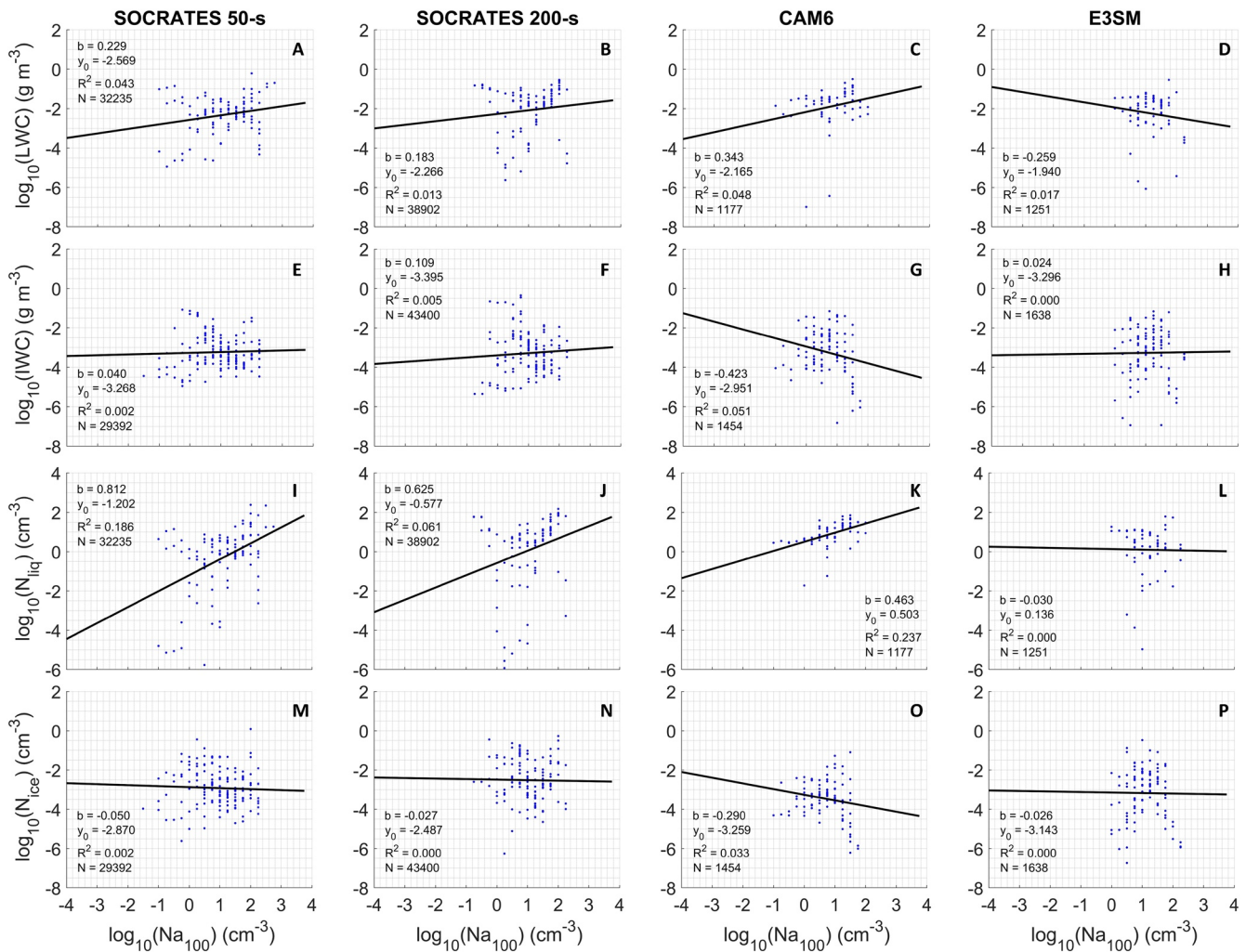
Figure 11. Similar to Figure 9 but applying linear regressions to cloud microphysical properties in relation to $\log_{10}(Na_{100})$.

For aerosol indirect effects of Na_{100} (Figure 11), CAM6 shows similar magnitudes of positive correlations with LWC ($b = 0.34$) and N_{liq} (0.46) compared with observations. However, CAM6 shows negative correlations with IWC (-0.42) and N_{ice} (-0.29) while the observations show no correlations. E3SM shows negative correlations with LWC ($b = -0.26$) and no correlations with IWC, N_{liq}, and N_{ice}. Overall, these results indicate that CAM6 is able to capture Twomey effect on liquid droplets from Na_{100} but not from Na_{500}, and it shows the opposite impacts on ice crystals from Na_{500} compared with observations. E3SM is able to capture a weak Twomey effect on ice crystals from Na_{500}, but underestimates Twomey effects on liquid droplets from Na_{500} and Na_{100}. In particular, both CAM6 and E3SM underestimate aerosol indirect effects on IWC.

Aerosol indirect effects on phase partitioning and cloud fraction are examined in Figure 12. The number of samples for Figure 12 is shown in Figure S11 in Supporting Information S1. Two types of glaciation ratios are examined—for all in-cloud conditions (Figures 12a–12h) and coexisting ice and liquid only (Figures 12i–12p). Since aerosols can serve as CCN and INPs as discussed above, the relationships between cloud fraction and aerosol number concentrations are also examined in Figures 12q–12x. Cloud fraction is calculated by normalizing the number of in-cloud samples in each bin by the total number of samples in that bin. Note that the cloud fraction for simulations is not based on the model output "cloud fraction" but rather is calculated based on the in-cloud definition described in Section 2.3. 100% cloudiness is seen in 50-s (200-s) observations at $Na_{500} > 3$ cm^{-3} (>0.3 cm^{-3}) and $Na_{100} > 300$ cm^{-3} (>100 cm^{-3}). On the other hand, the temperature effect is much stronger than aerosol indirect effects on cloud fraction in CAM6 and E3SM, with many model bins exceeding 70% cloudiness between $-15°C$ and $0°C$.
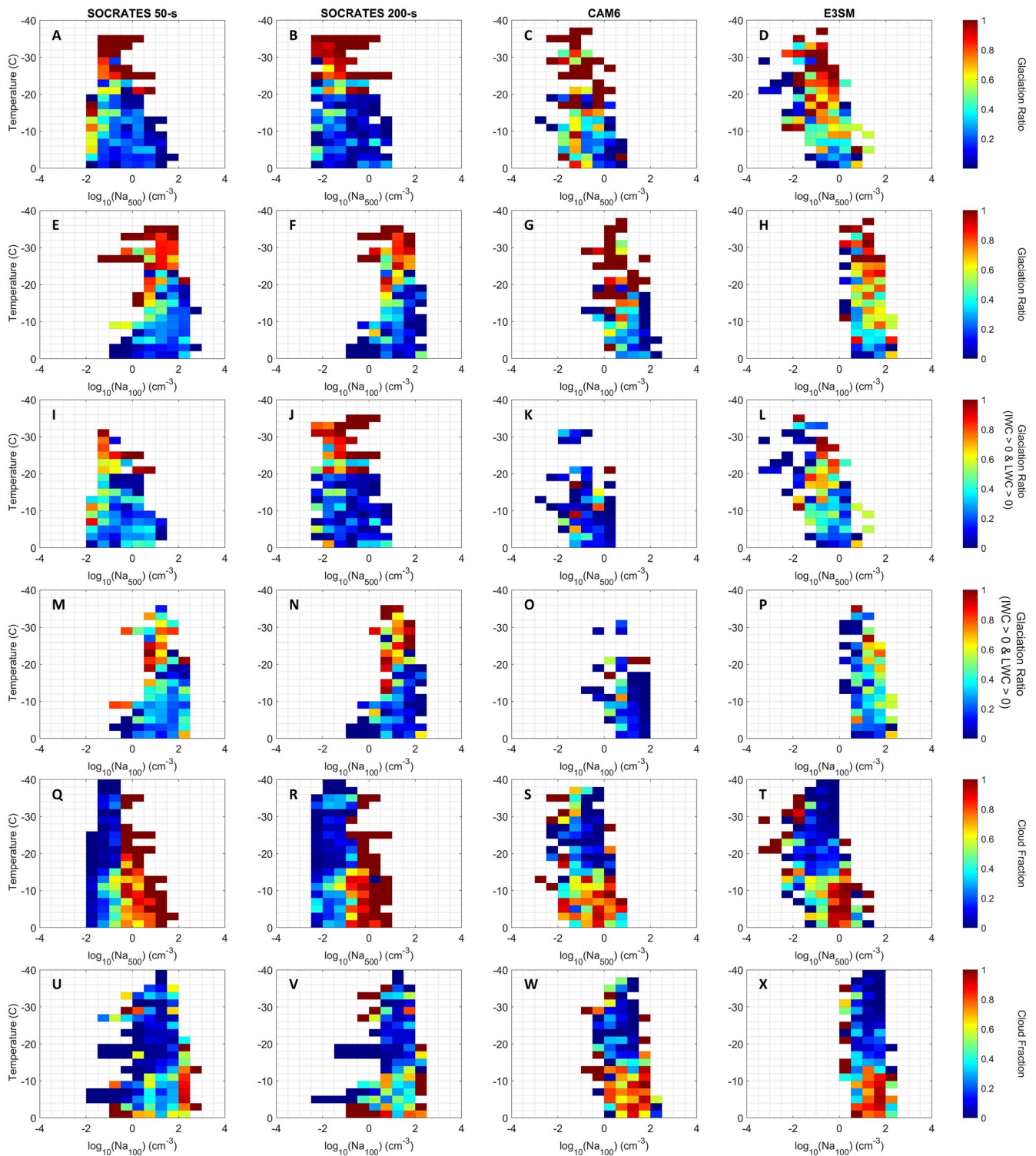
Figure 12. Relationships of (a–h) glaciation ratio of all clouds, (i–p) glaciation ratio only when ice particles and supercooled liquid water coexist, and (q–x) cloud fraction with respect to (rows 1, 3, and 5) $\log_{10}(Na_{500})$ and (rows 2, 4, and 6) $\log_{10}(Na_{100})$ at various temperatures. Columns 1–4 represent 50-s observations, 200-s observations, CAM6 and E3SM, respectively.
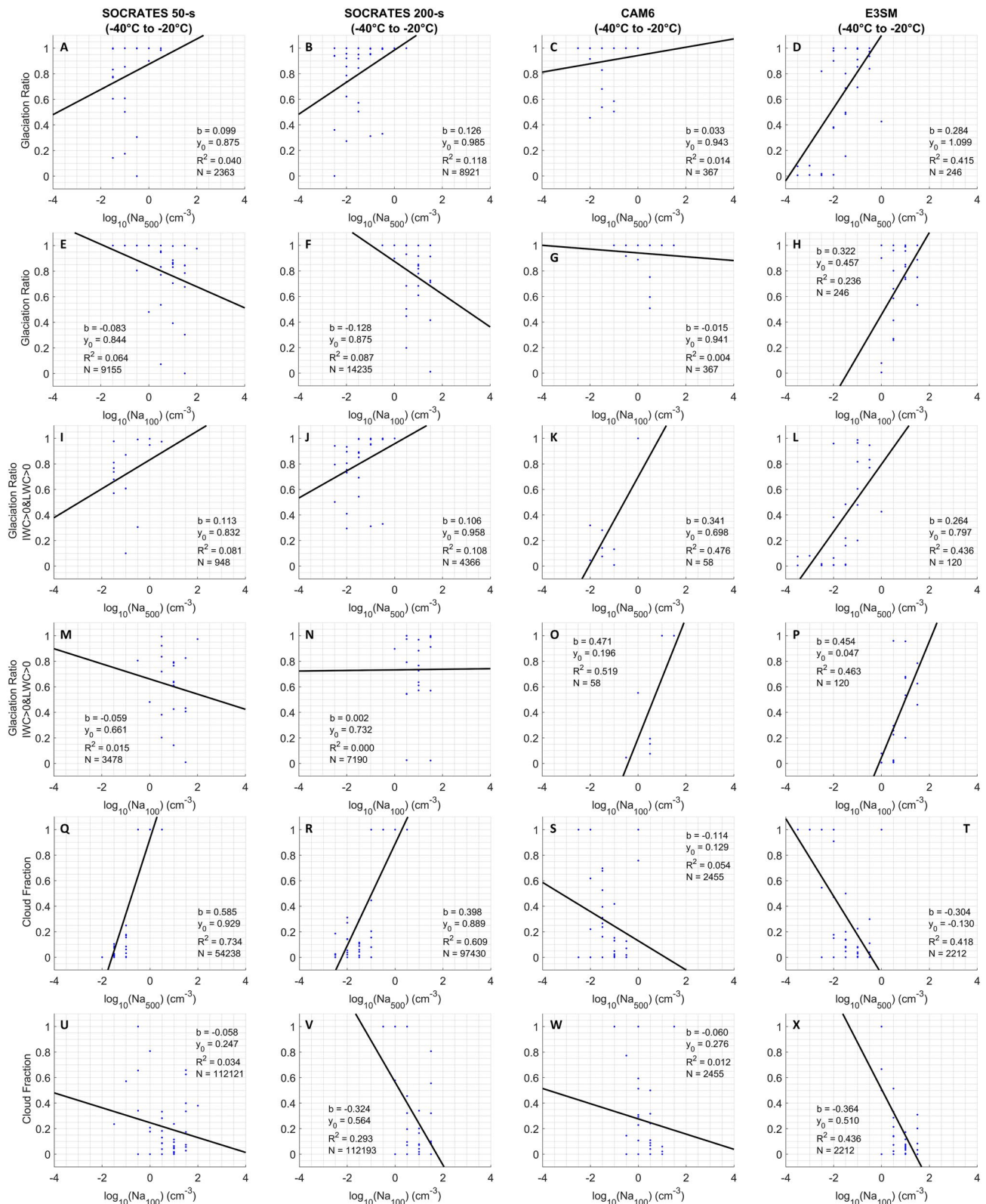
Figure 13. Linear regressions (black line) applied for (a–h) glaciation ratio of all clouds, (i–p) glaciation ratio only when ice particles and supercooled liquid water coexist, and (q–x) cloud fraction in relation to logarithmic scale aerosol number concentrations between −40°C and −20°C. Impacts of $\log_{10}(Na_{500})$ are shown in rows 1, 3, and 5. Impacts of $\log_{10}(Na_{100})$ are shown in rows 2, 4, and 6.
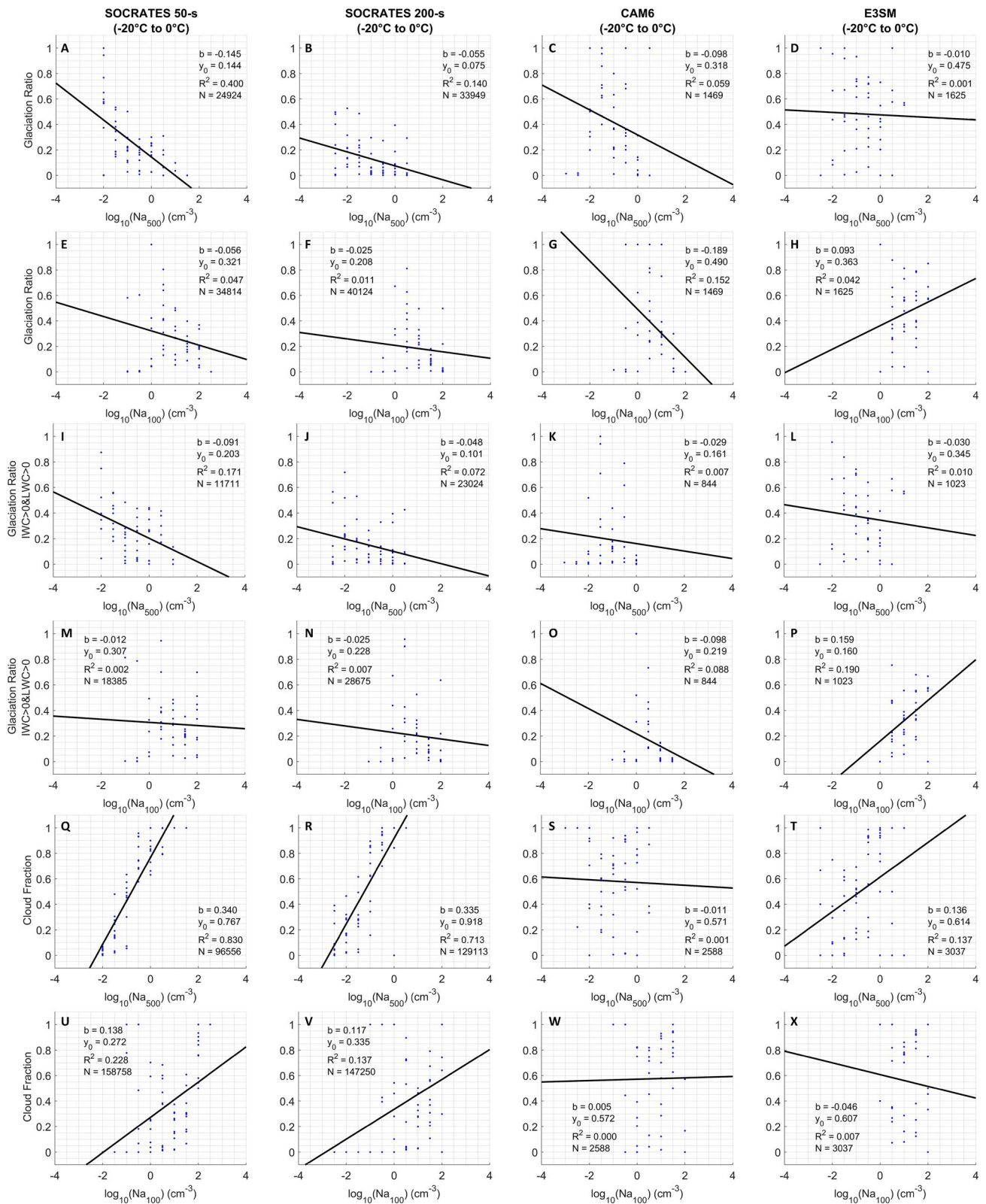
Figure 14. Similar to Figure 13 but for temperatures between −20°C and 0°C.

Two temperature ranges–between −40°C and 0°C and between −20°C and 0°C–show distinctive differences in aerosol indirect effects. Thus, we further examine the correlations of glaciation ratios and cloud fraction in relation to Na_{500} and Na_{100} in these two temperature ranges, separately (Figures 13 and 14). Linear regressions are applied to bin-average glaciation ratios and cloud fraction in relation to $\log_{10}(Na_{500})$ and $\log_{10}(Na_{100})$. In the lower temperature range of −40°C to −20°C, observations show positive correlations of two types of glaciation ratios and cloud fraction in relation to Na_{500}, and negative correlations of all three properties in relation to Na_{100}. This result indicates that at lower temperatures, larger aerosols are more effective in increasing IWC than increasing LWC, therefore glaciation ratios increase. Comparatively, smaller aerosols more effectively increase LWC and have almost no effects on IWC (Figure 11), therefore glaciation ratios decrease. Since cloud phase is dominated by ice phase at lower temperatures (Figure 3), higher Na_{500} means that more large aerosols can potentially serve as INPs, therefore cloud fraction also increases. On the other hand, since smaller aerosols are unlikely to serve as INPs, they may experience wet removal through precipitation, which possibly leads to the negative correlations between Na_{100} and cloud fraction. Both CAM6 and E3SM are able to capture increases of glaciation ratios with increasing Na_{500}. However, they both show negative correlations between Na_{500} and cloud fraction at the lower temperatures.

The main difference between the higher temperature range (−20°C to 0°C) and lower temperature range (−40°C to −20°C) is that the higher temperatures show similar impacts from Na_{500} and Na_{100} on glaciation ratios and cloud fraction, while the lower temperatures show opposite impacts from Na_{500} and Na_{100}. While Na_{500} and Na_{100} increase at the range of −20°C to 0°C, the two types of glaciation ratios decrease and cloud fraction increases. This result indicates that the enhancement of N_{liq} and LWC due to higher aerosol concentrations at the higher temperatures leads to less effective riming and secondary ice production, which results in lower glaciation ratios. Since cloud phase is dominated by liquid phase at this temperature range, the higher N_{liq} and LWC with higher Na contribute to higher cloud fraction, even though ice particle growth and secondary ice production decrease. Both CAM6 and E3SM are able to capture the negative correlations between Na_{500} and glaciation ratios, but only CAM6 captures the negative correlations between Na_{100} and glaciation ratios. E3SM captures the positive correlation between cloud fraction and higher Na_{500}, but shows a negative correlation between cloud fraction and Na_{100}. CAM6, however, does not show significant correlations of cloud fraction in relation to either Na_{500} or Na_{100}.

4. Conclusions and Implications to Model Development

This study focuses on examining cloud characteristics at −40°C to 0°C over the Southern Ocean based on in situ aircraft-based observations and three GCM simulations (i.e., CAM6, CAM5, and E3SM). A series of cloud characteristics are examined, including cloud phases, mass and number concentrations of cloud hydrometeors, phase partitioning, thermodynamic conditions, and aerosol indirect effects. Several approaches are used to facilitate the comparison between in situ observations and GCM simulations, including using nudged simulations toward reanalysis data, recalculating cloud properties based on instrument measurement ranges, and examining the impacts of spatial scales on the comparison results.

Spatially averaging observation data from 1 to 580 s (i.e., from ~0.2 to 100 km in horizontal) is found to affect several variables, such as reducing average LWC and IWC by 1–2 orders of magnitude due to the inclusion of clear-sky segments in the grid-mean averages, increasing the occurrence frequency of mixed phase clouds since ice particles and supercooled liquid water are more likely to coexist at coarser scales, reducing the maximum RH_{ice} for in-cloud and clear-sky conditions, and decreasing the peak positions of RH_{ice} PDFs for three cloud phases. For other characteristics, spatial averaging has a small impact on the average glaciation ratios of all in-cloud conditions, and the positive correlations of LWC, IWC, N_{liq}, and N_{ice} with respect to aerosol number concentrations.

Evaluation of three model simulations shows that CAM6 has the most similar cloud phase occurrence frequency to observations compared with CAM5 and E3SM. Particularly, CAM6 and E3SM significantly improve the proportion of liquid and mixed phase clouds below −15°C compared with CAM5. This is most likely due to the removal of a temperature-dependent mass partitioning function between ice and liquid in the shallow convection scheme (Park & Bretherton, 2009) that was previously used in CAM5, as discussed in previous studies (Gettelman et al., 2020; Kay et al., 2016). E3SM underestimates (overestimates) ice phase frequencies below (above) −20°C. When comparing simulated LWC with 580-s observations, CAM6 and E3SM overestimate LWC values

by 1–2 orders of magnitude below −25°C and −20°C, respectively. Another main model bias is the underestimation of IWC for CAM6 and E3SM below −25°C and −20°C, respectively, by 0.5–1 orders of magnitude compared with 580-s observations. Even though CAM6 shows small biases of glaciation ratios of all in-cloud conditions (i.e., with biases less than ±0.2), it significantly underestimates glaciation ratios of coexisting ice and liquid by 0.2–0.6 below −20°C due to the overestimation of LWC.

Thermodynamic conditions, specifically RH, were previously found to be well correlated with model biases of cloud occurrences and cloud phases (e.g., Wu et al., 2017). In terms of PDFs of in-cloud RH_{ice}, 1-s observations show larger variabilities of in-cloud RH_{ice} ranging from 3% to 147%, while the simulations show narrower ranges, that is, 20%–134% for CAM6, 52%–116% for CAM5, and 19%–144% for E3SM. When averaging the observations into every 580 s, the observed in-cloud RH_{ice} is seen from 7% to 132%, indicating that the simulations lack of sub-saturation at in-cloud conditions. This may limit the ranges of cloud microphysical properties, such as underestimating IWC by limiting ice growth and riming in sub-saturated conditions. Liu et al. (2018) previously showed that RH biases might be caused by local processes (i.e., boundary-layer turbulence, shallow, and deep convection) or even by biases in remote deep convection via water vapor advection. Therefore, future model development is recommended to examine the representations of these processes in the GCMs.

Regarding aerosol indirect effects on cloud microphysical properties, positive correlations are found between cloud microphysical properties (IWC, LWC, N_{ice}, and N_{liq}) and the number concentration of larger aerosols (Na_{500}) while only liquid properties (LWC and N_{liq}) are found to be positively correlated with the number concentration of smaller aerosols (Na_{100}) at various temperature ranges. This result suggests Twomey effects of larger aerosols on ice particles (i.e., possibly by acting as INPs) and supercooled liquid water (possibly by acting as CCN), while smaller aerosols only show Twomey effect on supercooled liquid water (possibly by acting as CCN). The increase of LWC and N_{liq} with increasing Na are stronger at warmer conditions (−20°C to 0°C) than colder conditions (−40°C to −20°C) in Figure 8, possibly due to less activation of ice nucleation at this temperature range and therefore less reduction of LWC and N_{liq} due to the WBF process. Aerosol indirect effects also show distinct features in the lower and higher temperature ranges, that is, −40°C to −20°C and −20°C to 0°C, respectively. At lower temperatures, Na_{500} seems to play a dominant role in controlling glaciation ratio via the glaciation indirect effect, that is, higher Na_{500} leads to higher INP concentrations, higher Nice and IWC, and consequently higher glaciation ratios and higher cloud fraction. At higher temperatures, the negative correlations between aerosol concentrations (both Na_{500} and Na_{100}) and glaciation ratios indicate that the riming indirect effects (i.e., more CCN, smaller droplets, less riming, and smaller IWC) and/or thermodynamic indirect effect (i.e., more CCN, more liquid droplets, and less secondary ice production) are possible pathways for aerosol indirect effects. Furthermore, since N_{ice} does not show strong correlation with Na_{100} (Figure 11m), the riming indirect effect is likely the dominant mechanism compared with the thermodynamic indirect effect at higher temperatures.

Small increases of LWC and N_{liq} with increasing Na are seen in CAM6 between −15°C and 0°C. Small increases of N_{ice} are seen in E3SM only at a narrow temperature range (−20°C to −10°C), and no increases of N_{ice} are seen in CAM6. In contrast to the observations, both models show stronger temperature effects on glaciation ratios and cloud fraction than aerosol indirect effects. These results suggest that stronger aerosol indirect effects on both liquid droplets and ice particles should be considered for future development of cloud microphysics parameterizations, especially since model parameterizations still have limited aerosol types acting as INPs. In addition, the maximum Na_{500} and Na_{100} values are underestimated in CAM6 and E3SM by 0.5–1 orders of magnitude compared with 200-s observations, suggesting that higher concentrations of INPs and CCN need to be included in the model. In fact, higher CCN number concentration has also been recommended in another model evaluation study on CAM6 by Gettelman et al. (2020).

Several caveats need to be noted for this study. First, for in situ observations, higher in-cloud thresholds (e.g., 0.01 g m^{-3} in McFarquhar et al., 2007 and 0.001 g m^{-3} in D'Alessandro et al., 2021) have been used to define clouds in previous studies, consistent with the definition of clouds as a visible collection of particles (Sassen & Campbell, 2001). But, due to the significant reduction of model sample sizes when these higher in-cloud thresholds are applied to simulated data, a lower threshold of 10^{-7} g m^{-3} is chosen for this study. A sensitivity test to the observations using in-cloud thresholds at 0.01 g m^{-3} (Figure 4d) shows similar cloud phase frequency distributions as the analysis using the threshold of 10^{-7} g m^{-3}. Second, the analysis of aerosol indirect effects separates the aerosols into larger and smaller sizes by using aerosols greater than 500 nm as a proxy of INPs based on the study of DeMott et al. (2010). However, that study did not include samples over the Southern Ocean,

and therefore the validity of the 500 nm threshold over this region still needs further investigation. Third, the measurements of aerosol size can be complicated by the drier sampling condition compared with the ambient condition, which reduces the size of aerosols. Due to the lack of aerosol composition measurements at 1-Hz resolution, such potential biases cannot be accurately corrected. However, it is unlikely that this potential bias of aerosol size measurements can explain all the relationships seen between Na_{500}, Na_{100}, and cloud microphysical properties (Figures 8–14).

Overall, this study provides a series of metrics for model evaluation of ice, liquid, and mixed phase clouds at $-40°C$ to $0°C$ based on high resolution, in situ observations. Both thermodynamic conditions and aerosol number concentrations are found to be important factors in controlling cloud phases, the mass partition of ice and liquid, and cloud hydrometeor mass and number concentrations. Diagnosis of the parameterizations that drive the model biases on cloud phases and cloud microphysical properties shown in this work is still warranted. The model evaluation in this study is restricted to default configurations of three GCMs, while future work is recommended to investigate the impacts of individual parameters in cloud microphysics parameterizations that may lead to improved results compared with observations. The observation-based statistical distributions of cloud phase frequency, microphysical properties, and their correlations with temperature, RH, and aerosol concentrations can be used to guide future model development at various horizontal scales.

Data Availability Statement

All aircraft observations can be obtained at https://data.eol.ucar.edu/. Three model simulations are stored in open archive at Mendeley Data, doi:10.17632/k9dyss9grs.1.

References

Baumgardner, D., & Korolev, A. (1997). Airspeed corrections for optical array probe sample volumes. *Journal of Atmospheric and Oceanic Technology*, *14*(5), 1224–1229. https://doi.org/10.1175/1520-0426(1997)014<1224:ACFOAP>2.0.CO;2

Bergeron, T. (1928). Über die dreidimensional verknüpfende Wetteranalyse. *Geophysica Norvegica*, *5*(7), 1–111. https://doi.org/10.1175/1520-0493(1931)59<275:TBBDDV>2.0.CO;2

Bodas-Salcedo, A., Hill, P. G., Furtado, K., Williams, K. D., Field, P. R., Manners, J. C., et al. (2016). Large contribution of supercooled liquid clouds to the solar radiation budget of the Southern Ocean. *Journal of Climate*, *29*, 4213–4228. https://doi.org/10.1175/JCLI-D-15-0564.1

Borys, R. D., Lowenthal, D. H., Cohn, S. A., & Brown, W. O. J. (2003). Mountaintop and radar measurements of anthropogenic aerosol effects on snow growth and snowfall rate. *Geophysical Research Letters*, *30*(10). https://doi.org/10.1029/2002gl016855

Bühl, J., Seifert, P., Engelmann, R., & Ansmann, A. (2019). Impact of vertical air motions on ice formation rate in mixed-phase cloud layers. *npj Climate and Atmospheric Science*, *2*(36). https://doi.org/10.1038/s41612-019-0092-6

Chen, T., Rossow, W. B., & Zhang, Y. (2000). Radiative effects of cloud-type variations. *Journal of Climate*, *13*(264–286). https://doi.org/10.1175/1520-0442(2000)013<0264:REOCTV>2.0.CO;2

Chubb, T., Huang, Y., Jensen, J., Campos, T., Siems, S., & Manton, M. (2016). Observations of high droplet number concentrations in Southern Ocean boundary layer clouds. *Atmospheric Chemistry and Physics*, *16*(2), 971–987. https://doi.org/10.5194/ACP-16-971-2016

D'Alessandro, J. J., Diao, M., Wu, C., Liu, X., Jensen, J. B., & Stephens, B. B. (2019). Cloud phase and relative humidity distributions over the Southern Ocean in austral summer based on in situ observations and CAM5 simulations. *Journal of Climate*, *32*(10), 2781–2805. https://doi.org/10.1175/JCLI-D-18-0232.1

D'Alessandro, J. J., McFarquhar, G. M., Wu, W., Stith, J. L., Jensen, J. B., & Rauber, R. M. (2021). Characterizing the occurrence and spatial heterogeneity of liquid, ice, and mixed phase low-level clouds over the Southern Ocean using in situ observations acquired during SOCRATES. *Journal of Geophysical Research: Atmospheres*, *126*(11), e2020JD034482. https://doi.org/10.1029/2020JD034482

DeMott, P. J., Prenni, A. J., Liu, X., Kreidenweis, S. M., Petters, M. D., Twohy, C. H., et al. (2010). Predicting global atmospheric ice nuclei distributions and their impacts on climate. *Proceedings of the National Academy of Sciences of the United States of America*, *107*(25), 11217–11222. https://doi.org/10.1073/pnas.0910818107

Diao, M. (2021). *VCSEL 1 Hz water vapor data*. UCAR/NCAR—Earth Observing Laboratory. Retrieved from https://data.eol.ucar.edu/dataset/552.051

Eidhammer, T., Morrison, H., Bansemer, A., Gettelman, A., & Heymsfield, A. J. (2014). Comparison of ice cloud properties simulated by the Community Atmosphere Model (CAM5) with in-situ observations. *Atmospheric Chemistry and Physics*, *14*, 10103–10118. https://doi.org/10.5194/acp-14-10103-2014

Field, P. R., Heymsfield, A. J., Shipway, B. J., DeMott, P. J., Pratt, K. A., Rogers, D. C., et al. (2012). Ice in clouds experiment–layer clouds. Part II: Testing characteristics of heterogeneous ice formation in lee wave clouds. *Journal of the Atmospheric Sciences*, *69*(3), 1066–1079. https://doi.org/10.1175/JAS-D-11-026.1

Fridlind, A. M., Ackerman, A. S., McFarquhar, G., Zhang, G., Poellot, M. R., DeMott, P. J., et al. (2007). Ice properties of single-layer stratocumulus during the mixed-phase Arctic Cloud Experiment: 2. Model results. *Journal of Geophysical Research*, *112*, D24202. https://doi.org/10.1029/2007JD008646

Gettelman, A., Bardeen, C., McCluskey, C. S., Järvinen, E., Stith, J., & Brethenton, C. (2020). Simulating observations of Southern Ocean clouds and implications for climate. *Journal of Geophysical Research*. https://doi.org/10.1002/essoar.10502322.1

Gettelman, A., & Morrison, H. (2015). Advanced two-moment bulk microphysics for global models. Part I: Off-line tests and comparison with other schemes. *Journal of Climate*, *28*(3), 1268–1287. https://doi.org/10.1175/JCLI-D-14-00102.1

Gierens, R., Kneifel, S., Shupe, M. D., Ebell, K., Maturilli, M., & Löhnert, U. (2020). Low-level mixed-phase clouds in a complex Arctic environment. *Atmospheric Chemistry and Physics*, *20*(6), 3459–3481. https://doi.org/10.5194/acp-20-3459-2020

Guo, Z., Wang, M., Peng, Y., & Luo, Y. (2020). Evaluation on the vertical distribution of liquid and ice phase cloud fraction in community atmosphere model version 5.3 using spaceborne lidar observations. *Earth and Space Science*, *7*, e2019EA001029. https://doi.org/10.1029/2019EA001029

Hallett, J. (2004). Measurement in the atmosphere In T. D. Potter, & B. R. Colman, (Eds.), *Handbook of weather, climate, and water: Dynamics, climate, physical meteorology, weather systems, and measurements* (pp. 711–720). John Wiley. https://doi.org/10.1002/0471721603.CH35

Hallett, J., & Mossop, S. C. (1974). Production of secondary ice particles during the riming process. *Nature*, *249*(5452), 26–28. https://doi.org/10.1038/249026a0

Jackson, R. C., McFarquhar, G. M., Korolev, A., Earle, M. E., Liu, P. S. K., Lawson, R. P., et al. (2012). The dependence of ice microphysics on aerosol concentration in arctic mixed-phase stratus clouds during ISDAC and M-PACE. *Journal of Geophysical Research*, *117*, D15207. https://doi.org/10.1029/2012JD017668

Kay, J. E., Hillman, B. R., Klein, S. A., Zhang, Y., Medeiros, B., Pincus, R., et al. (2012). Exposing global cloud biases in the community atmosphere model (CAM) using satellite observations and their corresponding instrument simulators. *Journal of Climate*, *25*(15), 5190–5207. https://doi.org/10.1175/JCLI-D-11-00469.1

Kay, J. E., Wall, C., Yettella, V., Medeiros, B., Hannay, C., Caldwell, P., & Bitz, C. (2016). Global climate impacts of fixing the Southern Ocean shortwave radiation bias in the community Earth System model (CESM). *Journal of Climate*, *29*(12), 4617–4636. https://doi.org/10.1175/JCLI-D-15-0358.1

Klein, S. A., Mccoy, R. B., Morrison, H., Ackerman, A. S., Avramov, A., De Boer, G., et al. (2009). Intercomparison of model simulations of mixed-phase clouds observed during the ARM Mixed-Phase Arctic Cloud Experiment. I: Single-layer cloud. *Quarterly Journal of the Royal Meteorological Society*, *135*, 979–1002. https://doi.org/10.1002/qj.416

Korolev, A., & Field, P. R. (2008). The effect of dynamics on mixed-phase clouds: Theoretical considerations. *Journal of the Atmospheric Sciences*, *65*, 66–86. https://doi.org/10.1175/2007JAS2355.1

Korolev, A., & Isaac, G. (2003). Phase transformation of mixed-phase clouds. *Quarterly Journal of the Royal Meteorological Society*, *129*(587), 19–38. https://doi.org/10.1256/qj.01.203

Korolev, A., McFarquhar, G., Field, P. R., Franklin, C., Lawson, P., Wang, Z., et al. (2017). Mixed-phase clouds: Progress and challenges. *Meteorological Monographs*, *58*, 5–15. https://doi.org/10.1175/amsmonographs-d-17-0001.1

Lin, S.-J. (2004). A "vertically Lagrangian" finite-volume dynamical core for global models. *Monthly Weather Review*, *132*, 2293–2307. https://doi.org/10.1175/1520-0493(2004)132<2293:AVLFDC>2.0.CO;2

Liou, K. N. (1992). *Radiation and cloud processes in the atmosphere* (pp. 255–339). Oxford University Press.

Liu, Q., Jia, X., Quan, J., Li, J., Li, X., Wu, Y., et al. (2018). New positive feedback mechanism between boundary layer meteorology and secondary aerosol formation during severe haze events. *Scientific Reports*, *8*(11), 1–8. https://doi.org/10.1038/s41598-018-24366-3

Liu, X., Easter, R. C., Ghan, S. J., Zaveri, R., Rasch, P., Shi, X., et al. (2012). Toward a minimal representation of aerosols in climate models: Description and evaluation in the Community Atmosphere Model CAM5. *Geoscientific Model Development*, *5*(3), 709–739. https://doi.org/10.5194/gmd-5-709-2012

Liu, X., Ma, P. L., Wang, H., Tilmes, S., Singh, B., Easter, R. C., et al. (2016). Description and evaluation of a new four-mode version of the modal aerosol module (MAM4) within version 5.3 of the community atmosphere model. *Geoscientific Model Development*, *9*(2), 505–522. https://doi.org/10.5194/gmd-9-505-2016

Lohmann, U. (2002). Possible aerosol effects on ice clouds via contact nucleation. *Journal of the Atmospheric Sciences*, *59*, 647–656. https://doi.org/10.1175/1520-0469(2001)059<0647:PAEOIC>2.0.CO;2

Lohmann, U., Henneberger, J., Henneberg, O., Fugal, J. P., Bühl, J., & Kanji, Z. A. (2016). Persistence of orographic mixed-phase clouds. *Geophysical Research Letters*, *43*(1910), 512519–512610. https://doi.org/10.1002/2016GL071036

Matus, A. V., & L'Ecuyer, T. S. (2017). The role of cloud phase in Earth's radiation budget. *Journal of Geophysical Research: Atmospheres*, *122*(5), 2559–2578. https://doi.org/10.1002/2016JD025951

Mazin, I. P., Korolev, A., Heymsfield, A., Isaac, G. A., & Cober, S. G. (2001). Thermodynamics of icing cylinder for measurements of liquid water content in supercooled clouds. *Journal of Atmospheric and Oceanic Technology*, *18*(4), 543–558. https://doi.org/10.1175/1520-0426(2001)018<0543:TOICFM>2.0.CO;2

McCoy, D. T., Tan, I., Hartmann, D. L., Zelinka, M. D., & Storelvmo, T. (2016). On the relationships among cloud cover, mixed-phase partitioning, and planetary albedo in GCMs. *Journal of Advances in Modeling Earth Systems*, *8*(2), 650–668. https://doi.org/10.1002/2015MS000589

McFarquhar, G. M., Bretherton, C. S., Marchand, R., Protat, A., DeMott, P. J., Alexander, S. P., et al. (2021). Observations of clouds, aerosols, precipitation, and surface radiation over the Southern Ocean: An overview of CAPRICORN, MARCUS, MICRE, and SOCRATES. *Bulletin of the American Meteorological Society*, *102*(4), E894–E928. https://doi.org/10.1175/BAMS-D-20-0132.1

McFarquhar, G. M., & Heymsfield, A. J. (2001). Parameterizations of INDOEX microphysical measurements and calculations of cloud susceptibility: Applications for climate studies. *Journal of Geophysical Research*, *106*, 28675–28698. https://doi.org/10.1029/2000JD900777

McFarquhar, G. M., Zhang, G., Poellot, M. R., Kok, G. L., McCoy, R., Tooman, T., et al. (2007). Ice properties of single-layer stratocumulus during the mixed-phase Arctic Cloud Experiment: 1. Observations. *Journal of Geophysical Research*, *112*(D24), 24201. https://doi.org/10.1029/2007JD008633

Morrison, A. E., Siems, S. T., Manton, M. J., & Nazarov, A. (2010). A modeling case study of mixed-phase clouds over the Southern Ocean and Tasmania. *Monthly Weather Review*, *138*(3), 839–862. https://doi.org/10.1175/2009MWR3011.1

Morrison, H., & Gettelman, A. (2008). A new two-moment bulk stratiform cloud microphysics scheme in the community atmosphere model, version 3 (CAM3). Part I: Description and numerical tests. *Journal of Climate*, *21*(15), 3642–3659. https://doi.org/10.1175/2008JCLI2105.1

Mülmenstädt, J., Sourdeval, O., Delanoë, J., & Quaas, J. (2015). Frequency of occurrence of rain from liquid-, mixed-, and ice-phase clouds derived from A-Train satellite retrievals. *Geophysical Research Letters*, *42*(15), 6502–6509. https://doi.org/10.1002/2015GL064604

Murphy, D. M., & Koop, T. (2005). Review of the vapour pressures of ice and supercooled water for atmospheric applications. *Quarterly Journal of the Royal Meteorological Society*, *131*(608), 1539–1565. https://doi.org/10.1256/qj.04.94

Neale, R. B., Chen, C.-C., Gettelman, A., Lauritzen, P. H., Park, S., Williamson, D. L., et al. (2012). *Description of the NCAR Community Atmosphere Model (CAM 5.0)* (Vol. 486, p. 268). NCAR Technical Note.

Park, S., & Bretherton, C. S. (2009). The University of Washington shallow convection and moist turbulence schemes and their impact on climate simulations with the community atmosphere model. *Journal of Climate*, *22*(12), 3449–3469. https://doi.org/10.1175/2008JCLI2557.1

Patnaude, R., Diao, M., Liu, X., & Chu, S. (2021). Effects of thermodynamics, dynamics and aerosols on Cirrus clouds based on in situ observations and NCAR CAM6 model. *Atmospheric Chemistry and Physics*, *21*(3), 1835–1859. https://doi.org/10.5194/acp-21-1835-2021

Qiu, S., Xi, B., & Dong, X. (2018). Influence of wind direction on thermodynamic properties and arctic mixed-phase clouds in autumn at Utqiaġvik, Alaska. *Journal of Geophysical Research: Atmospheres*, *123*(17), 9589–9603. https://doi.org/10.1029/2018JD028631

Rangno, A. L., & Hobbs, P. V. (2001). Ice particles in stratiform clouds in the Arctic and possible mechanisms for the production of high ice concentrations. *Journal of Geophysical Research: Atmospheres*, *106*(D14), 15065–15075. https://doi.org/10.1029/2000JD900286

Rasch, P. J., Xie, S., Ma, P.-L., Lin, W., Wang, H., Tang, Q., et al. (2019). An overview of the atmospheric component of the energy Exascale Earth System Model. *Journal of Advances in Modeling Earth Systems*, *11*(8), 2377–2411. https://doi.org/10.1029/2019MS001629

Sassen, K., & Campbell, J. R. (2001). A midlatitude cirrus cloud climatology from the facility for atmospheric remote sensing. Part I: Macrophysical and synoptic properties. *Journal of the Atmospheric Sciences*, *58*(5), 481–496. https://doi.org/10.1175/1520-0469(2001)058<0481:AMCCCF>2.0.CO;2

Shupe, M. D., Kollias, P., Persson, P. O. G., & McFarquhar, G. M. (2008). Vertical motions in arctic mixed-phase stratiform clouds. *Journal of the Atmospheric Sciences*, *65*, 1304–1322. https://doi.org/10.1175/2007JAS2479.1

Storelvmo, T., Hoose, C., & Eriksson, P. (2011). Global modeling of mixed-phase clouds: The albedo and lifetime effects of aerosols. *Journal of Geophysical Research*, *116*(D5), D05207. https://doi.org/10.1029/2010JD014724

Sun, J., Zhang, K., Wan, H., Ma, P., Tang, Q., & Zhang, S. (2019). Impact of nudging strategy on the climate representativeness and hindcast skill of constrained EAMv1 simulations. *Journal of Advances in Modeling Earth Systems*, *11*(12), 3911–3933. https://doi.org/10.1029/2019MS001831

Tan, I., & Storelvmo, T. (2016). Sensitivity study on the influence of cloud microphysical parameters on mixed-phase cloud thermodynamic phase partitioning in CAM5. *Journal of the Atmospheric Sciences*, *73*(2), 709–728. https://doi.org/10.1175/JAS-D-15-0152.1

Tan, I., Storelvmo, T., & Zelinka, M. D. (2016). Observational constraints on mixed-phase clouds imply higher climate sensitivity. *Science*, *352*, 224–227. https://doi.org/10.1126/science.aad5300

Trenberth, K. E., & Fasullo, J. T. (2010). Simulation of present-day and twenty-first-century energy budgets of the southern oceans. *Journal of Climate*, *23*(2), 440–454. https://doi.org/10.1175/2009JCLI3152.1

Wang, Y., McFarquhar, G. M., Rauber, R. M., Zhao, C., Wu, W., Finlon, J. A., et al. (2020). Microphysical properties of generating cells over the Southern Ocean: Results from SOCRATES. *Journal of Geophysical Research: Atmospheres*, *125*(13). https://doi.org/10.1029/2019JD032237

Wegener, A. (1911). Thermodynamik der Atmosphäre. *Nature*, *90*(2237), 31. https://doi.org/10.1038/090031a0

Williams, K. D., Bodas-Salcedo, A., Déqué, M., Fermepin, S., Medeiros, B., Watanabe, M., et al. (2013). The transpose-AMIP II experiment and its application to the understanding of Southern Ocean cloud biases in climate models. *Journal of Climate*, *26*, 3258–3274. https://doi.org/10.1175/JCLI-D-12-00429.1

Wood, R., Kuan-Ting, O., Bretherton, C. S., Mohrmann, J., Albrecht, B. A., Zuidema, P., et al. (2018). Ultraclean layers and optically thin clouds in the stratocumulus-to-cumulus transition. Part I: Observations. *Journal of the Atmospheric Sciences*, *75*(5), 1631–1652. https://doi.org/10.1175/JAS-D-17-0213.1

Wu, C., Liu, X., Diao, M., Zhang, K., Gettelman, A., Lu, Z., et al. (2017). Direct comparisons of ice cloud macro- and microphysical properties simulated by the Community Atmosphere Model version 5 with HIPPO aircraft observations. *Atmospheric Chemistry and Physics*, *17*, 4731–4749. https://doi.org/10.5194/acp-17-4731-2017

Wu, W., & McFarquhar, G. M. (2016). On the impacts of different definitions of maximum dimension for nonspherical particles recorded by 2D imaging probes. *Journal of Atmospheric and Oceanic Technology*, *33*(5), 1057–1072. https://doi.org/10.1175/JTECH-D-15-0177.1

Zaremba, T. J., Rauber, R. M., McFarquhar, G. M., Hayman, M., Finlon, J. A., & Stechman, D. M. (2020). Phase characterization of cold sector Southern Ocean cloud tops: Results from SOCRATES. *Journal of Geophysical Research: Atmospheres*, *125*(24). https://doi.org/10.1029/2020JD033673

Zhang, M., Liu, X., Diao, M., D'Alessandro, J. J., Wang, Y., Wu, C., et al. (2019). Impacts of representing heterogeneous distribution of cloud liquid and ice on phase partitioning of arctic mixed-phase clouds with NCAR CAM5. *Journal of Geophysical Research: Atmospheres*, *124*(23), 13071–13090. https://doi.org/10.1029/2019JD030502

Zhang, M., Xie, S., Liu, X., Lin, W., Zhang, K., Ma, H., et al. (2020). Toward understanding the simulated phase partitioning of arctic single-layer mixed-phase clouds in E3SM. *Earth and Space Science*, *7*(7). https://doi.org/10.1029/2020ea001125

Zhang, Y., Xie, S., Lin, W., Klein, S. A., Zelinka, M., Ma, P., et al. (2019). Evaluation of clouds in version 1 of the E3SM atmosphere model with satellite simulators. *Journal of Advances in Modeling Earth Systems*, *11*(5), 1253–1268. https://doi.org/10.1029/2018MS001562

Zondlo, M. A., Paige, M. E., Massick, S. M., & Silver, J. A. (2010). Vertical cavity laser hygrometer for the National Science Foundation Gulfstream-V aircraft. *Journal of Geophysical Research*, *115*(D20), D20309. https://doi.org/10.1029/2010JD014445